Delft University of Technology

Dual polarimetric radar vegetation index for crop growth monitoring using sentinel-1 SAR data

Mandal, Dipankar; Kumar, Vineet; Ratha, Debanshu; Dey, Subhadip; Bhattacharya, Avik; Lopez-Sanchez, Juan M.; McNairn, Heather; Rao, Yalamanchili S.

DOI
10.1016/j.rse.2020.111954

Publication date
2020

Document Version
Final published version

Published in
Remote Sensing of Environment

Citation (APA)
Mandal, D., Kumar, V., Ratha, D., Dey, S., Bhattacharya, A., Lopez-Sanchez, J. M., McNairn, H., & Rao, Y. S. (2020). Dual polarimetric radar vegetation index for crop growth monitoring using sentinel-1 SAR data. *Remote Sensing of Environment*, *247*, Article 111954. https://doi.org/10.1016/j.rse.2020.111954

Important note
To cite this publication, please use the final published version (if applicable).
Please check the document version above.

Copyright
Other than for strictly personal use, it is not permitted to download, forward or distribute the text or part of it, without the consent of the author(s) and/or copyright holder(s), unless the work is under an open content license such as Creative Commons.

Takedown policy
Please contact us and provide details if you believe this document breaches copyrights.
We will remove access to the work immediately and investigate your claim.

This work is downloaded from Delft University of Technology.
For technical reasons the number of authors shown on this cover page is limited to a maximum of 10.

Remote Sensing of Environment 247 (2020) 111954

Contents lists available at ScienceDirect

Remote Sensing of Environment

journal homepage: www.elsevier.com/locate/rse

Dual polarimetric radar vegetation index for crop growth monitoring using sentinel-1 SAR data

Dipankar Mandal[a,*], Vineet Kumar[a,b], Debanshu Ratha[a], Subhadip Dey[a], Avik Bhattacharya[a], Juan M. Lopez-Sanchez[c], Heather McNairn[d], Yalamanchili S. Rao[a]

[a] *Microwave Remote Sensing Lab, Centre of Studies in Resources Engineering, Indian Institute of Technology Bombay, Mumbai, India*
[b] *Department of Water Resources, Delft University of Technology, Delft, the Netherlands*
[c] *Institute for Computer Research, University of Alicante, Alicante, Spain*
[d] *Ottawa Research and Development Centre, Agriculture and Agri-Food Canada, Ottawa, Canada*

ARTICLE INFO

Keywords:
Canola
Degree of polarization
RVI
PAI
DpRVI
Vegetation water content

ABSTRACT

Sentinel-1 Synthetic Aperture Radar (SAR) data have provided an unprecedented opportunity for crop monitoring due to its high revisit frequency and wide spatial coverage. The dual-pol (VV-VH) Sentinel-1 SAR data are being utilized for the European Common Agricultural Policy (CAP) as well as for other national projects, which are providing Sentinel derived information to support crop monitoring networks. Among the Earth observation products identified for agriculture monitoring, indicators of vegetation status are deemed critical by end-user communities. In literature, several experiments usually utilize the backscatter intensities to characterize crops. In this study, we have jointly utilized the scattering information in terms of the degree of polarization and the eigenvalue spectrum to derive a new vegetation index from dual-pol (DpRVI) SAR data. We assess the utility of this index as an indicator of plant growth dynamics for canola, soybean, and wheat, over a test site in Canada. A temporal analysis of DpRVI with crop biophysical variables (viz., Plant Area Index (PAI), Vegetation Water Content (VWC), and dry biomass (DB)) at different phenological stages confirms its trend with plant growth dynamics. For each crop type, the DpRVI is compared with the cross and co-pol ratio ($\sigma_{VH}{}^{0}/\sigma_{VV}{}^{0}$) and dual-pol Radar Vegetation Index (RVI = $4\sigma_{VH}{}^{0}/(\sigma_{VV}{}^{0} + \sigma_{VH}{}^{0})$), Polarimetric Radar Vegetation Index (PRVI), and the Dual Polarization SAR Vegetation Index (DPSVI). Statistical analysis with biophysical variables shows that the DpRVI outperformed the other four vegetation indices, yielding significant correlations for all three crops. Correlations between DpRVI and biophysical variables are highest for canola, with coefficients of determination (R^2) of 0.79 (PAI), 0.82 (VWC), and 0.75 (DB). DpRVI had a moderate correlation ($R^2 \gtrsim 0.6$) with the biophysical parameters of wheat and soybean. Good retrieval accuracies of crop biophysical parameters are also observed for all three crops.

1. Introduction

Monitoring crop condition is a principal factor for estimating and forecasting production. When agencies require continuous monitoring of crop production over large spatial extents, mapping from space offers an effective option. Although optical remote sensing has been successfully used (Boryan et al., 2011; de Wit et al., 2012; López-Lozano et al., 2015; Chipanshi et al., 2015) in several operational frameworks (e.g., MODIS vegetation products), useful acquisitions by this type of sensors are restricted to nearly cloud-free conditions. In this context, synthetic aperture radar (SAR) data are of significant interest for agricultural applications due to the ability of SAR systems to monitor under all weather conditions, as well as the sensitivity of the microwave signal to the dielectric and geometrical properties crops (Ulaby, 1975; McNairn and Shang, 2016). In particular, the availability of dual-pol SAR datasets from the Sentinel-1 mission provides unique opportunities to ramp up operational monitoring for several application communities (ESA, 2017). Dual-pol modes have advantages over full-pol acquisitions in terms of larger swath width and less data volume at the expense of limited polarimetric information (Lee et al., 2001; Ainsworth et al., 2009), offering some benefits for agencies in ongoing operational activities.

The Sentinel-1 dual-pol mode (VV-VH), refers to the transmission of a vertically polarized wave with the simultaneous reception of vertical

---

[*] Corresponding author.
E-mail address: dipankar_mandal@iitb.ac.in (D. Mandal).

https://doi.org/10.1016/j.rse.2020.111954
Received 31 January 2020; Received in revised form 9 June 2020; Accepted 12 June 2020
0034-4257/ © 2020 Elsevier Inc. All rights reserved.

and horizontal polarization. Hence, the received wave in co- and cross-polarized channels (VV-VH) provides information about a target in terms of backscatter intensities. Several studies utilized the backscatter intensities for identification of crop types (Kussul et al., 2016; Nguyen et al., 2016; Bargiel, 2017; Van Tricht et al., 2018; Mandal et al., 2018; Whelen and Siqueira, 2018; Arias et al., 2020) and crop biophysical parameter estimation (Bousbih et al., 2017; Kumar et al., 2018; Mandal et al., 2020a). The sensitivity of backscatter intensities to crop phenology and morphological development led to developing crop monitoring approaches solely with scattering powers (Nelson et al., 2014; De Bernardis et al., 2015; Nguyen et al., 2016; Lasko et al., 2018; Singha et al., 2019; Fikriyah et al., 2019).

Several researchers have investigated derivation of vegetation metrics from SAR data using backscatter intensity ratios. Blaes et al. (2006) investigated the sensitivity of $\sigma_{\mathrm{VH}}{}^{0}/\sigma_{\mathrm{VV}}{}^{0}$ against the growth dynamics of maize. At incidence angles of 35–45°, $\sigma_{\mathrm{VV}}{}^{0}/\sigma_{\mathrm{VH}}{}^{0}$ was sensitive to plant growth until the leaf area index (LAI) and vegetation water content (VWC) reached 4.9 $\mathrm{m}^2\ \mathrm{m}^{-2}$) and 5.6 kg m^{-2}, respectively. Later, this ratio is applied to crop classification (McNairn et al., 2009; Inglada et al., 2016; Denize et al., 2019), phenology estimation (McNairn et al., 2018; Canisius et al., 2018), and vegetation characterization (Veloso et al., 2017; Vreugdenhil et al., 2018; Khabbazan et al., 2019). Veloso et al. (2017) noted that this ratio was relatively stable during pre-cultivation stages and increased significantly at the tillering stages of cereal crops (wheat and barley). The $\sigma_{\mathrm{VH}}{}^{0}/\sigma_{\mathrm{VV}}{}^{0}$ ratio was better correlated to the fresh biomass of cereals and the Normalized Difference Vegetation Index (NDVI), compared to individual channel backscatter response. Besides, this ratio provided better separability among maize, soybean, and sunflower during their heading/flowering stages.

The quad-pol Radar Vegetation Index (RVI) proposed by Kim and van Zyl (2009), was modified for dual-pol SAR data (Trudel et al., 2012) as $4\sigma_{\mathrm{HV}}{}^{0}/(\sigma_{\mathrm{HH}}{}^{0} + \sigma_{\mathrm{HV}}{}^{0})$. Later, few studies used the alternative formulation as $4\sigma_{\mathrm{VH}}{}^{0}/(\sigma_{\mathrm{VV}}{}^{0} + \sigma_{\mathrm{VH}}{}^{0})$ using Sentinel-1 dual-pol data (VV-VH) (Nasirzadehdizaji et al., 2019; Gururaj et al., 2019). These approaches are driven by the utilization of the cross-polarized component of the received wave. Periasamy (2018) proposed the Dual Polarization SAR Vegetation Index (DPSVI) by investigating the physical scattering behaviour of several targets (vegetation, soil, urban area, and water) in co- and cross-pol channels of Sentinel-1. It calculates the rate of depolarization in terms of the vertical dual depolarization index, $(\sigma_{\mathrm{VV}}{}^{0} + \sigma_{\mathrm{VH}}{}^{0})/\sigma_{\mathrm{VV}}{}^{0}$ to separate bare soil from vegetation. The DPSVI had R^2 values greater than 0.70 with both optical NDVI and above-ground biomass. Chang et al. (2018) exploited the degree of polarization parameter (average of HH and VV channel degree of polarizations) along with the cross-pol backscatter intensity to characterize vegetation and bare soil. It may be noted that utilizing the scattered wave information in terms of the roll-invariant degree of polarization (m) would enhance target characterization (Shirvany et al., 2012; Touzi et al., 2015, 2018).

Chang et al. (2018) utilized the degree of polarization of partially polarized waves for deriving a vegetation index (PRVI) for quad-pol SAR data. Assuming the vegetation canopy as a depolarizing media, they first obtained the depolarized part by subtracting the degree of polarization from unity (i.e., $(1 - m)$), subsequently multiplying it with the cross-polarization channel intensity ($\sigma_{HV}{}^{0}$ in dB). This approach delivered good correlation of shrubland biomass with PRVI ($R^2 = 0.75$) than RVI ($R^2 = 0.50$). Shrubby vegetation usually develops random structures within the canopy. However, agricultural crops often exhibit a predefined orientation (e.g., vertical or horizontal based on erectophiles and planophiles) and crops are typically sown in rows. In this sense, relying on only cross-polarized power may lead to issues related to backscatter intensity saturation. Hence, including HV (or VH) may falsely indicate a high value of the vegetation index, even though the vegetation canopy is not entirely developed. An alternative would be to exploit the dominant scattering component (in terms of the eigenvalue spectrum of the covariance matrix) while calculating the polarized components.

In the present work, we utilize the dual-pol Sentinel-1 SAR data to derive a new radar vegetation index, named as dual-pol radar vegetation index (DpRVI) for crop condition monitoring. The eigenvalue spectrum obtained from the eigen-decomposition of the dual-pol covariance matrix and the degree of polarization is used to derive this new index. Instead of including the polarization channel backscatter intensities (Chang et al., 2018; Periasamy, 2018), the proposed index uses the normalized dominant eigenvalue and the degree of polarization which are roll and polarization basis invariant. Moreover, DpRVI is a bounded quantity (between 0 and 1), unlike PRVI, which uses the channel intensity in decibel, making it unbounded. We assess the performance of the DpRVI as an indicator of plant growth dynamics over the Joint Experiment for Crop Assessment and Monitoring (JECAM) test site in Carman (Manitoba), Canada. We perform a comparative analysis between DpRVI, $\sigma_{\mathrm{VH}}{}^{0}/\sigma_{\mathrm{VV}}{}^{0}$, dual-pol RVI, PRVI, and DPSVI for three structurally diverse crop types. We further assess the temporal response of DpRVI to vegetation dynamics by comparing them with the in-situ measured vegetation biophysical parameters, including Plant Area Index (PAI), Vegetation Water Content (VWC), and Dry biomass (DB).

2. Study area and dataset

The present study is carried over the Joint Experiment for Crop Assessment and Monitoring (JECAM) test site in Carman, Manitoba (Canada), as shown in Fig. 1. This site covers an area of intensive agriculture of 26 × 48 km^2. A diverse mix of annual crops is grown in this region, with dominant crops including wheat, canola, soybeans, corn, and oats. Only a small fraction ($< 5\%$) is under permanent grassland and pasture. The in-situ measurements were collected over the area near coincident with satellite passes during the Soil Moisture Active Passive Validation Experiment 2016 Manitoba (SMAPVEX16-MB) campaign (Bhuiyan et al., 2018).

During the campaign, in-situ measurements of vegetation and soil were collected in two distinct periods (June 08 to June 22, and July 8 to July 22, 2016) over 50 agricultural fields. During this experimental period, most of the crops advanced from an early stage of growth following emergence to peak accumulation of biomass, as shown in Fig. 2. The nominal size of each field is approximately 800 m × 800 m. In each sampling field, three points were selected for vegetation sampling, as shown in Fig. 1, which included measurement of plant area index (PAI), wet and dry biomass, plant height, and phenological stages using both destructive and non-destructive sampling methods (Bhuiyan et al., 2018). The biomass measurements are used to derive the vegetation water content (VWC) and dry biomass (DB) per unit square meter area.

Details of the vegetation and soil sampling methods during the field campaign can be found in the SMAPVEX16-MB report in McNairn et al. (2016) and in Bhuiyan et al. (2018). From several Sentinel-1 images acquired during the campaign, four dual-polarization (VV and VH) C-band Sentinel-1A Single Look Complex (SLC) data are selected for use in this study (Table 1). The selection of Sentinel-1 data is based on acquisition dates near coincident with in-situ measurement periods.

3. Methodology

3.1. SAR data preprocessing

Sentinel-1 acquires data over land majorly in the Terrain Observation with Progressive Scans SAR (TOPSAR) mode and delivers the Level-1 SLC data in an Interferometric Wide (IW) product. A full swath is approximately 250 km in length at 5 × 20 m spatial resolution in single look. The IW swath consists of three sub-swaths (IW1, IW2, and IW3) in the range direction. Each sub-swaths has 9 bursts in the azimuth direction, and the individually focused complex bursts are arranged in azimuth-time order with black-fill in between. For further

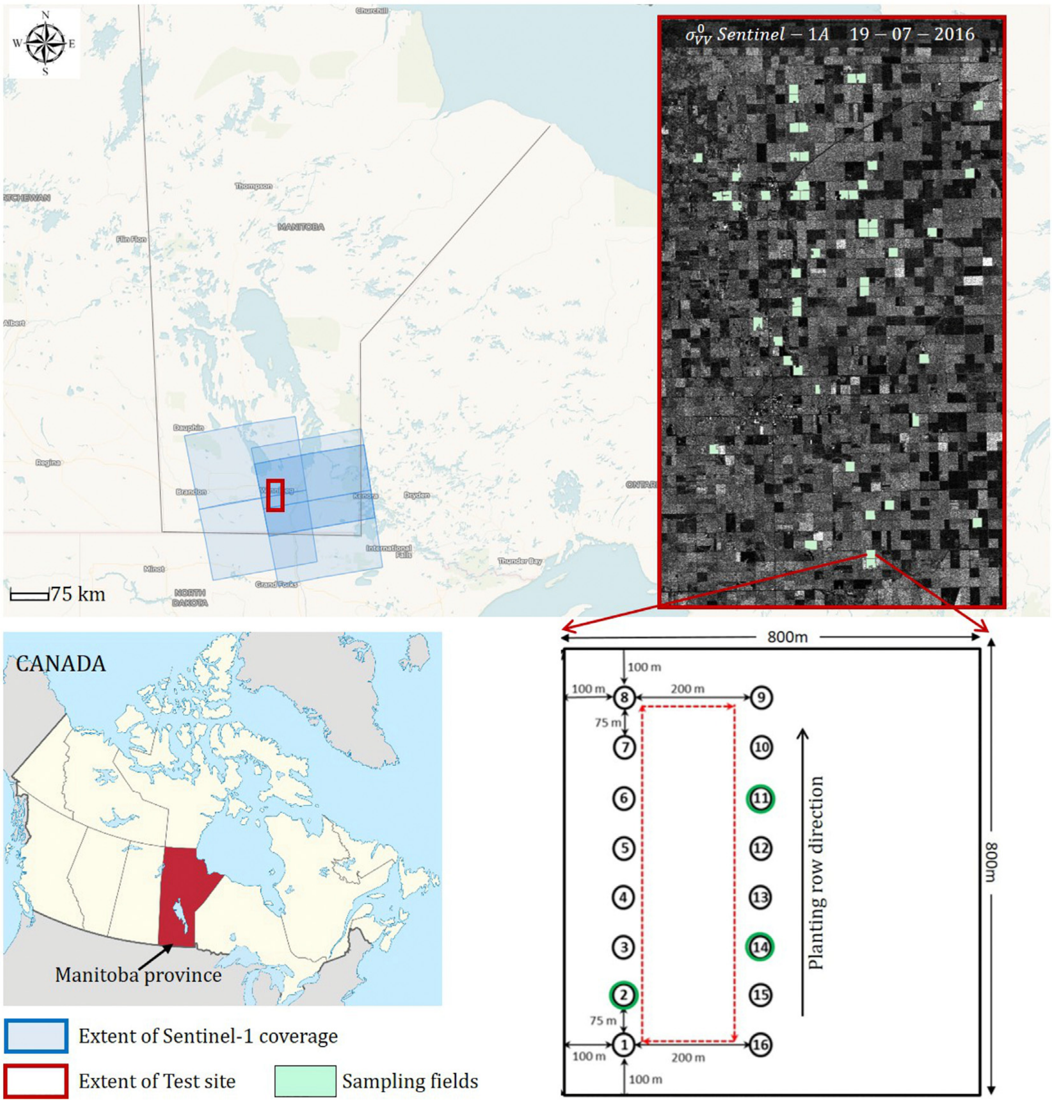
N
W
E
S
Churchill
Thompson
MANITOBA
Flin Flon
Albert
Dauphin
Regina
Brandon
Kenora
Dryden
ONTARIO
International Falls
Thunder Bay
Minot
NORTH DAKOTA
Grand Forks
75 km
σ^0_{VV} Sentinel − 1A 19 − 07 − 2016
CANADA
Manitoba province
Extent of Sentinel-1 coverage
Extent of Test site
Sampling fields
800m
800m
100 m
100 m
200 m
75 m
75 m
200 m
100 m
100 m
1
2
3
4
5
6
7
8
9
10
11
12
13
14
15
16
Planting row direction

Fig. 1. Study area (red box) and Sentinel-1 passes (blue boxes) over the Carman JECAM test site. The sample fields (mint green polygons) are overlayed on $\sigma_{VV}{}^0$ Sentinel-1A image of 19 July, 2016. A layout of 16 sampling locations within a field is highlighted. (For interpretation of the references to colour in this figure legend, the reader is referred to the web version of this article.)

applications, these SLC products are preprocessed with a standard set of corrections in a workflow, as shown in Fig. 3.

This study involves preprocessing of the temporal dataset to obtain the dual-pol 2 × 2 covariance matrices. Individual Sentinel-1 images are read into the SNAP7.0 tool (ESA, 2015). The sub-swaths and bursts are then selected based on the test area coverage with the TOPS Split module. A precise orbit file is applied to update the state vectors, and subsequently, the images are calibrated. Unlike the Ground Range Detected (GRD) processing pipeline, which is used to generate the radar cross-section powers (σ^0), the current workflow requires saving the radiometric calibration output product in a complex-valued format. A complex-values output is necessary to generate the covariance matrix in succeeding steps. These processing steps are performed in a batch mode for all temporal datasets.

All these calibrated images from different dates are coregistered with sub-pixel accuracy using a digital elevation model (DEM) and orbit information in SNAP 'Sentinel-1 Back Geocoding' operator. For the current work, we have utilized the SRTM 1Sec Grid (approximately 30 m pixel size) as DEM. Subsequently, the stack of temporal images is processed for Sentinel-1 TOPS Deburst and TOPS Merge, which merges different bursts of an individual image (of a particular date) into a single SLC image. Subset operation is then performed on the debursted image to clip the product into a smaller spatial extent covering the test area.

The subset stacked images are multilooked by 4 × 1 in range and azimuth direction to generate ground ranged square pixels. These multi-looked products are then utilized to produce a 2 × 2 covariance matrix ($\mathbf{C}_2$). The matrix elements are further processed by despeckling them with a 5 × 5 refined Lee filter. It may be noted that in this study, the nominal size of each plot is ~ 800 m × 800 m and fields are chosen as homogeneous as possible according to the agronomic practices. The 5 × 5 window is selected to ensure enough equivalent number of looks (ENL) for a good estimation of the elements of DpRVI.

The next step requires the deletion of baseline information from the metadata, which is essential for exporting the covariance matrices from SNAP to the PolSARPro format. The stack is then split into individual products using the Stack Split operator, and these products (i.e., the 2 × 2 covariance matrices for single dates) are exported into the PolSARPro format. Each matrix element (C_{11}, C_{22}, $\Re(C_{12})$, and $\Im(C_{12})$) is stored individually in a binary format with separate header information. These elements essentially deal with the second-order scattering information generated from the spatial averaging of the

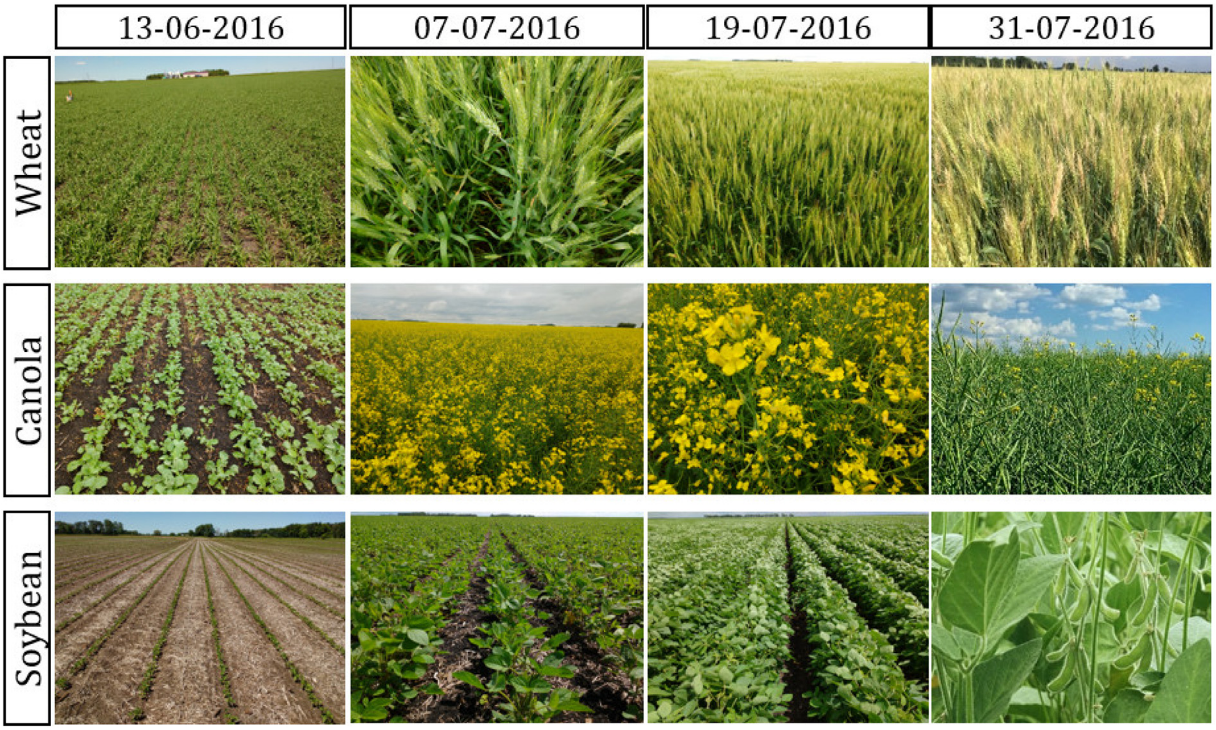

Fig. 2. Field conditions for wheat, canola, and soybean crops during the SMAPVEX16-MB campaign.

scattering vector $k = [S_{VV}, S_{VH}]^T$ as expressed in (1),

$$\mathbf{C}_2 = \begin{bmatrix} C_{11} & C_{12} \\ C_{21} & C_{22} \end{bmatrix} = \begin{bmatrix} \langle |S_{VV}|^2 \rangle & \langle S_{VV} S_{VH}^* \rangle \\ \langle S_{VH} S_{VV}^* \rangle & \langle |S_{VH}|^2 \rangle \end{bmatrix} \tag{1}$$

where superscript * denotes complex conjugate and $\langle \cdots \rangle$ denotes the spatial average over a moving window.

The DpRVI is then generated from the covariance matrix elements for each date. These images are subsequently geocoded to a UTM projected coordinate systems using the Range Doppler Terrain correction. Further analysis is performed with the in-situ measurement locations and extracted radar vegetation index from the geocoded products.

3.2. Dual-pol radar vegetation index (DpRVI)

Radar backscatter intensity provides information about spatial and temporal variations in crop growth and changes in their phenology stages (Lopez-Sanchez et al., 2014). Exploiting the characteristics of scattering randomness from vegetation structures, radar vegetation indices have been proposed including RVI (Kim and van Zyl, 2009), RVII-RVIII (Szigarski et al., 2018), GRVI (Mandal et al., 2020b), and CpRVI (Mandal et al., 2020c) for full- and compact-pol SAR data. These SAR indices were developed to provide a relatively simple and physically interpretable vegetation descriptor. Although these radar vegetation indices are good proxies for vegetation condition, they are confined to the use of full or compact polarimetric SAR data. A vegetation index based on dual-pol SAR data (viz., Sentinel-1) would be advantageous for operational crop monitoring over expansive geographies.

In this study, we have jointly utilized the scattering information in terms of the degree of polarization and the eigenvalue spectrum to derive a new vegetation index from dual-pol SAR data. The state of polarization of an EM wave is characterized in terms of the degree of polarization ($0 \leq m \leq 1$). The degree of polarization is defined as the ratio of the (average) intensity of the polarized portion of the wave to that of the (average) total intensity of the wave. For a completely polarized EM wave, $m = 1$ and for a completely unpolarized EM wave, $m = 0$. In between these two extreme cases, the EM wave is considered to be partially polarized, $0 < m < 1$. In the literature, the unpolarized part of the received wave, $(1 - m)$ is usually considered to represent the volume scattering component from distributed targets (Raney et al., 2012).

Barakat (Barakat, 1977) provided an expression of m for the $N \times N$ covariance matrix. This expression is used in this study to obtain the degree of polarization m from the 2×2 covariance matrix $\mathbf{C}_2$ for dual-pol data as,

$$m = \sqrt{1 - \frac{4|\mathbf{C}_2|}{(\mathrm{Tr}(\mathbf{C}_2))^2}} \tag{2}$$

where Tr is the matrix trace operator (i.e., the sum of the diagonal elements) and $|\cdot|$ is the determinant of a matrix.

In addition, the two non-negative eigenvalues ($\lambda_1 \geq \lambda_2 \geq 0$) are obtained from the eigen-decomposition of the $\mathbf{C}_2$ matrix which are then normalized with the total power Span ($\mathrm{Tr}(\mathbf{C}_2) = \lambda_1 + \lambda_2$). The eigenvalues quantify the dominancy of scattering mechanisms. For a

Table 1
Sentinel-1A acquisitions over Carman test site during SMAPVEX16-MB campaign (IW: Interferometric Wide swath). The incidence angle ranges shown here are over the test area of 26×48 km^2.

Satellite data acquisition date	Beam mode	Incidence angle range (deg.)	Orbit	In-situ measurement window
13-06-2016	IW	30.22–32.47	Ascending	13-06-2016 15-06-2016
07-07-2016	IW	30.22–32.44	Ascending	05-07-2016 06-07-2016
19-07-2016	IW	30.22–32.44	Ascending	17-07-2016 20-07-2016
31-07-2016	IW	39.82–41.79	Ascending	Not Available

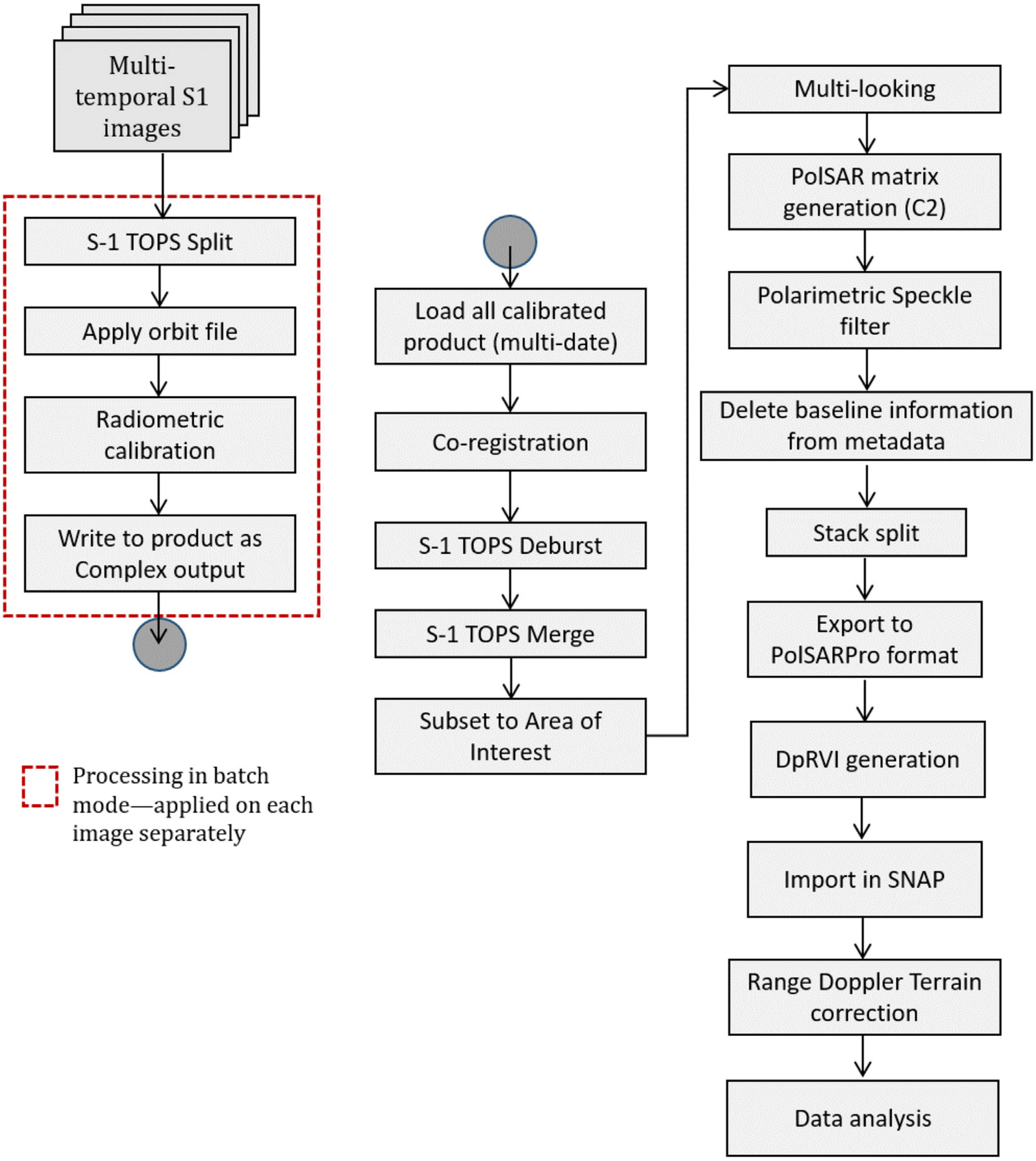
Multi-temporal S1 images
S-1 TOPS Split
Apply orbit file
Radiometric calibration
Write to product as Complex output
Processing in batch mode—applied on each image separately
Load all calibrated product (multi-date)
Co-registration
S-1 TOPS Deburst
S-1 TOPS Merge
Subset to Area of Interest
Multi-looking
PolSAR matrix generation (C2)
Polarimetric Speckle filter
Delete baseline information from metadata
Stack split
Export to PolSARPro format
DpRVI generation
Import in SNAP
Range Doppler Terrain correction
Data analysis

Fig. 3. Sentinel-1 preprocessing workflow for time-series data.

single dominant scattering mechanism, $\lambda_1 \gg \lambda_2$. Moreover, in dual-pol, m is equivalent to wave anisotropy, which quantifies the relative strength among the first and the second dominant scattering mechanisms. Therefore, in this study, we utilize the parameter $\beta = \lambda_1/\text{Span}$ as a measure of dominancy in the scattering mechanism.

Most studies solely consider the cross-polarized channel (i.e., VH or HV) intensity to characterize scattering from random structures. For most distributed targets, VV and HH are dominated by first-order scattering (i.e., direct backscatter with no multiple reflections), whereas HV (or VH) is due to second- and higher-order scattering (i.e., two or more reflections involving two or more scatterers). Unlike the PRVI (Chang et al., 2018), which utilizes the degree of polarization and the HV backscatter coefficient (i.e., $\sigma_{HV}{}^{0}$) from full-polarimetric SAR data, the proposed formulation for the dual-pol radar vegetation index (DpRVI) introduces a measure of dominancy via the β parameter.

The dominant scattering information is modulated with the degree of polarization (m), which in particular characterizes anisotropy for dual-pol SAR data. The scattering randomness is then obtained by subtracting $m\beta$ from unity, as given in (3).

$$\text{DpRVI} = 1 - m\beta, \quad 0 \le \text{DpRVI} \le 1, \tag{3}$$

Besides, multiplying of the VH component directly to other components of PRVI and DPSVI makes then unbounded (Periasamy, 2018; Chang et al., 2018). Unlike PRVI and DPSVI, the utilization of the normalized of the dominant eigenvalue (i.e., λ_1/Span) makes it bounded between 0 and 1, which is useful and natural to interpret considering the lower and upper bounds owning physical significance. Besides, the normalized dominant eigenvalue and the degree of polarization are both roll and polarization basis invariant.

Equivalently, an alternative formulation would be to have the product of $(1 - m)$ and λ_2/Span. It may be noted that this is analogous to the formulation of PRVI (Chang et al., 2018), which is a product of $(1 - m)$ and $\sigma_{HV}{}^{0}$. Here $(1 - m)$ is the unpolarized part of the scattered wave and λ_2/Span indicates the less dominant scattering term. However, λ_2/Span is intrinsically noisier rather than depicting actual changes in scattering randomness from vegetation canopy.

It is apparent from Fig. 4 that the standard deviation of λ_2/Span increases as canola advances from the leaf development stage (13 June) to pod development and maturity (3rd week of July). The mean value of λ_2/Span increases with plant growth stages while following an inverse trend with λ_1/Span. The structural heterogeneity of plants during the

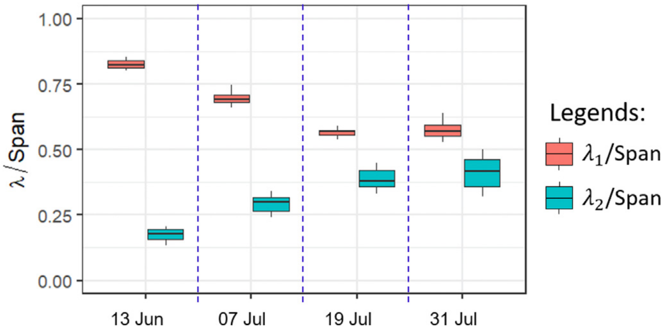

Fig. 4. Temporal pattern of normalized eigenvalue (λ_1/Span and λ_2/Span) derived from coherency matrix ($\mathbf{C}_2$) for canola fields.

reproductive to maturity stage might lead to a spatial variance within a parcel. Hence, this might increases variation in DpRVI values from mean at advanced growth stages.

Furthermore, it is noteworthy that the standard deviation of λ_1/Span is relatively lower than λ_2/Span and the mean value decreases with plant growth stages. Hence, the product of m and β corresponds to the scaling of the dominant scattering. Order of scattering increases as crop canopy develops. At the initial stages of crop development (early leaf development), usually, the scattering from the soil surface is dominant. However, at the advanced vegetative stage, multiple scattering from the canopy and soil is more apparent. Hence, m is expected to decrease from early to advanced vegetative stage. It may be noted that a similar sensitivity of the degree of polarization is highlighted with increasing order of scattering (Chang and Shoshany, 2017; Chang et al., 2018).

Furthermore, the principal basis to couple m and β is inferred from their differential sensitivity to crop growth dynamics. The experimental plots that are shown in Fig. 5 indicate their variations through temporal growth stages for three different crops.

Even though these parameters are investigated in detail in Section 4, here, we briefly highlight their importance to characterize the proposed index. This insight is particularly vital considering that even though these two parameters show analogous trends, they exhibit differential variations within a distinctive dynamic range at several phenological stages. For example, the mean values of m and β decrease with the growth stages of canola (Fig. 5). It is interesting to note that both m and β are > 0.70 with a marginal difference between their values on 13 June. However, m and β diverge as canola phenology advances until full vegetative growth is attained during mid-July. Similarly, for soybean and wheat, the differential sensitivities of m and β are apparent throughout its growth stages, as shown in Fig. 5. It is interesting to note that unlike other crops, wheat shows an increasing trend in both m and β during the end of the ripening stage on 31 July, with higher variations in responses of both parameters. These differences may be due to a high degree of randomness in scattering from wheat heads or due to a drier canopy which allows greater contribution from the soil.

It can be observed from the general analysis of the eigenvalue spectrum (given in Appendix A) that these differential variations between m and β are related to λ_2/Span. This measure which quantifies the less dominant scattering mechanism is inappreciable when $m \approx 1$, and unreliable due to large variance with increasing scattering randomness. In most circumstances, at the early stage of plant development, there exists a single dominant scattering mechanism usually from the bare soil. This is manifested by a low difference between m and β. A decrease in the uncertainty among two targets is controlled by the mutual use of m and β.

The elements of DpRVI (i.e., m and β) are shown in a polar plot (Fig. 6). It may be noted that we have utilized the parameter β in the linear scale in the formulation of DpRVI (Eq. (3)). The angular representation of this parameter is solely utilized to represent it in the polar plot (Fig. 6) along with m. This particular type of representation is adopted in this study to adequately perceive subtle variations of DpRVI due to the diversity in the scattering characteristics through the transition of phenological stages. In this plot, $\cos^{-1}\beta$ is represented in the angular direction, while m is plotted in the radial axis. It can be noted that $\cos^{-1}\beta$ varies from 0 to 60° in the angular direction, while m radially varies from 0 to 1.

The polar plot is used to illustrate temporal variations in the scattering attributes for each crop type, individually discriminated by m and β. Some canonical or elementary targets are also shown, which are located at the extremes of the boundaries, while natural targets reside within the polar plot.

The β parameter indicates the contribution of the dominant scattering component within the total backscattered power. For pure or point target scattering with a dominant scattering mechanism, $\beta = 1$ which assigns to $\cos^{-1}\beta = 0^{\circ}$ with $m = 1$ in the polar plot. This state corresponds to Case-2 shown in Fig. 6 with DpRVI = 0. Theoretically, for a smooth bare surface (i.e., Bragg scattering), $\lambda_1 \gg \lambda_2$ with a high value of m pointing to $\cos^{-1}\beta \approx 0$. However, the cluster density plot of bare soil indicates variations in m and $\cos^{-1}\beta$ about their theoretical positions, which are due to the natural variability in real scenarios.

In the case of completely random scattering (i.e., with no polarization structure), $m = 0$ (i.e., completely depolarized wave) and $\beta = 0.5$. This suggests that $\lambda_1 = \lambda_2 =$ Span/2 for which DpRVI = 1. Case-1 is a typical example of such a state. For natural targets like fully developed vegetation canopy, $m \approx 0$ and $\beta \approx 0.5$, leading to higher DpRVI, i.e., DpRVI ≈ 1. Moreover, dispersion of m and β in the density

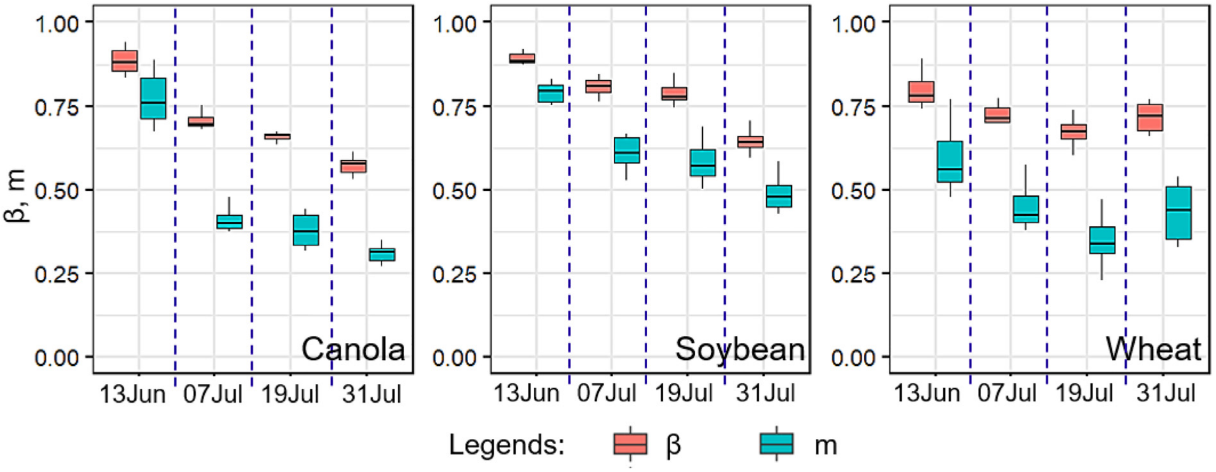

Fig. 5. Sensitivity of m and β parameters through the growing season for canola, soybean, and wheat crops.

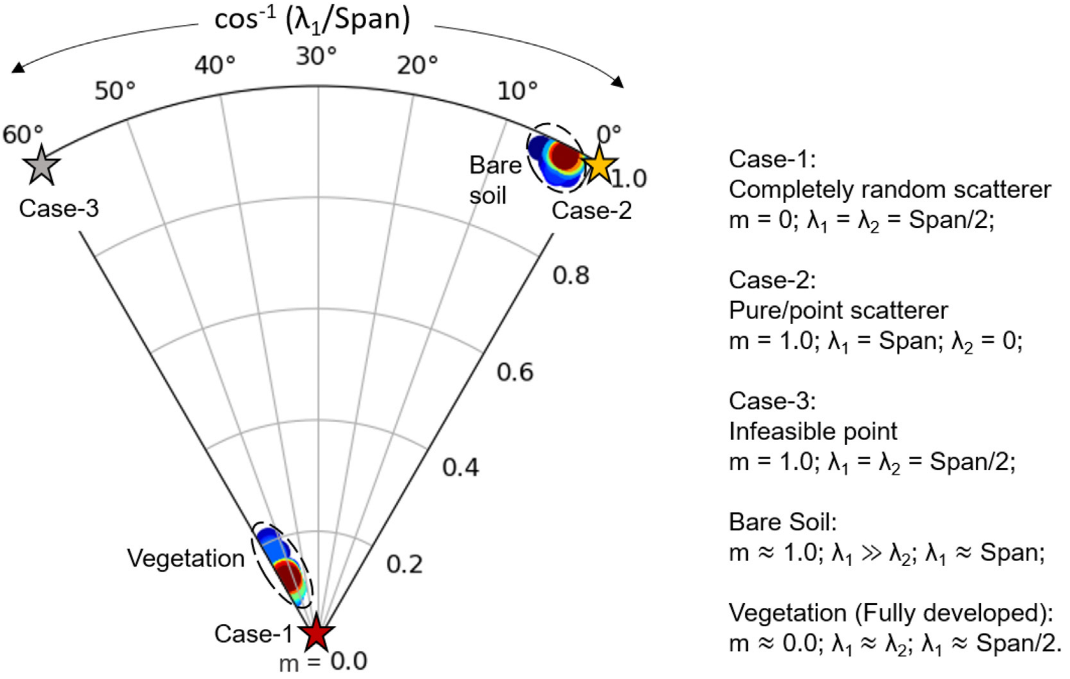

Fig. 6. The elements of DpRVI i.e., degree of polarization (m) and β (i.e., λ_1/Span) in polar plot. The $\cos^{-1}\beta$ is represented in the angular direction and m in radial axis of the polar plot. The boundary cases and regions of natural targets are highlighted. The vegetation and soil clusters are derived using radar measurements over the sampling fields.

plot is evident in the vegetation cluster. As plant canopy advances from early leaf development to fully vegetative stage, the DpRVI increases from 0 to 1.

It can be noted that at each phenological stage, m and β are represented as points in the polar plot. However, certain regions in the $m-\beta$ plot are infeasible due to the non-existence of physical depolarizers in such regions. Case-3 is an instance of such a state, where $m = 1.0$ (i.e., pure target) and $\cos^{-1}\beta = 60^{\circ}$, indicating, $\lambda_1 = \lambda_2 = \text{Span}/2$ (i.e., similar to a complete depolarizer). These types of targets are not practically possible in natural scenarios.

3.3. Data analysis and comparison

Elements of the $\mathbf{C}_2$ matrix are used to calculate the DpRVI as discussed in Section 3, for each acquisition over a 5 × 5 window. In addition, the DpRVI is compared with the cross and co-pol ratio ($\sigma_{VH}{}^0/\sigma_{VV}{}^0$), RVI ($4\sigma_{\text{VH}}{}^0/(\sigma_{\text{VV}}{}^0 + \sigma_{\text{VH}}{}^0)$), PRVI and DPSVI. The $\sigma_{VH}{}^0/\sigma_{VV}{}^0$ and RVI are computed from the diagonal elements of the $\mathbf{C}_2$ matrix. The in-situ measurement points are overlaid on the temporal $\sigma_{VH}{}^0/\sigma_{VV}{}^0$, RVI, PRVI, DPSVI and DpRVI images. Here it is important to note that the nominal field size of the study area is relatively larger (approx. 800m × 800m) than the size of the image pixel (approx. 15m × 15m). Hence, the vegetation indices for each sampling location are calculated as an average over a 3 × 3 window centered on each site.

It should be noted that the dual-pol RVI and PRVI are not fundamental for dual-pol systems. The full-pol Radar Vegetation Index (RVI) was formulated by modeling the vegetation canopy as a collection of randomly oriented dipoles (Kim and van Zyl, 2009), and in principle utilizes a measure of scattering randomness from vegetation targets and formulated from eigenvalue spectrum of full-pol covariance matrix $\mathbf{C}_3$. However, for dual-pol, RVI formulation is approximated from the final formulation of the full-pol RVI. On the other hand, the PRVI in principle is not directly comparable to the DpRVI as the former is proposed for full-pol SAR data (Chang et al., 2018). The degree of polarization is derived using the modified Mueller matrix with Stokes parameters, assuming a completely and linearly polarized transmitted wave. However, the DpRVI is directly comparable to DPSVI and $\sigma_{\text{VH}}{}^0/\sigma_{\text{VV}}{}^0$, which are created from dual-pol SAR data. Nonetheless, for completeness and relevant analysis, we have included the comparison of DpRVI with related radar vegetation indices like PRVI, dual-pol RVI, $\sigma_{\text{VH}}{}^0/\sigma_{\text{VV}}{}^0$, and DPSVI.

These parameters are initially investigated on a temporal scale for various phenological stages of crops. We have selected three structurally different crops for this study: wheat, canola, and soybean. The temporal behaviour of these parameters are also compared with crop biophysical variables, such as the Plant Area Index (PAI, m^2m^{-2}), dry biomass (DB, kg m^{-2}), and vegetation water content (VWC, kg m^{-2}). Finally, the DpRVI, $\sigma_{VH}{}^0/\sigma_{VV}{}^0$, RVI, PRVI, and DPSVI are utilized in a correlation analysis with these crop biophysical variables.

4. Results and discussion

This section describes the results of the proposed vegetation index–DpRVI separately for three crop types, viz., canola, soybean, and wheat. The results of the statistical comparison of the five indices: DpRVI, $\sigma_{VH}{}^0/\sigma_{VV}{}^0$, dual-pol RVI, PRVI and DPSVI with the three crop parameters, PAI, DB, and VWC, are also documented in this section.

4.1. Canola

The temporal analysis of DpRVI averaged for three sampling points in each canola fields (Field no. 206, 208, and 224) is provided in Fig. 7. For comparison, $\sigma_{VH}{}^0/\sigma_{VV}{}^0$, dual-pol RVI, PRVI and DPSVI are presented in the same figure. Furthermore, a regression analysis is performed for the vegetation indices with in-situ measured PAI, VWC, and dry biomass (Fig. 9).

The in-situ measurements indicate that canola seeding was almost completed by the 3rd week of May. Thus, plant development during the beginning of June was primarily limited to vegetative growth. Subsequently, flowering started in the last week of June to early July, which led to pod development by the middle of July. Ripening of seeds and senescence followed at the end of July until the 2nd week of August. The phenological stages are highlighted in the temporal plots of vegetation indices for each field (Fig. 7).

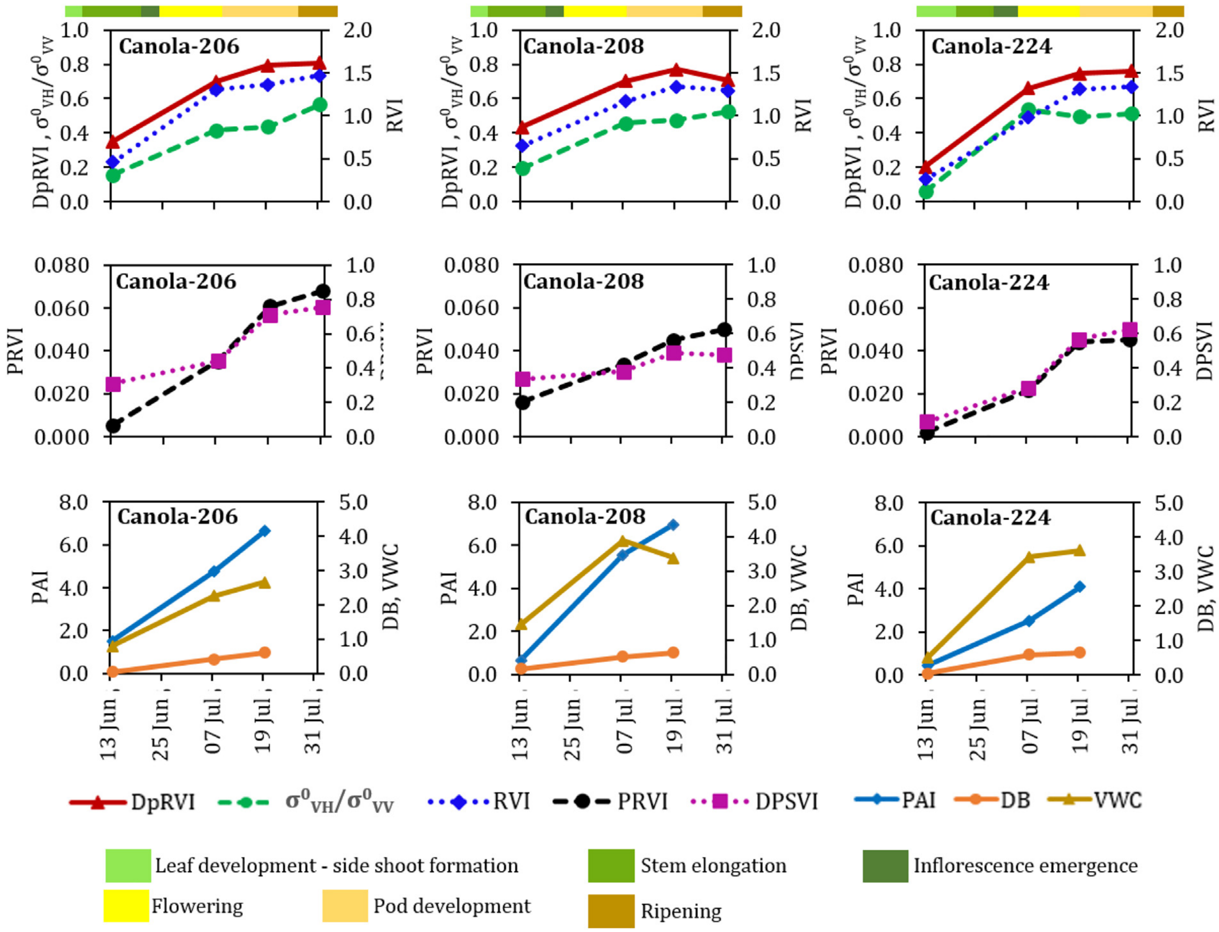

Fig. 7. Temporal pattern of vegetation indices (DpRVI, $\sigma_{VH}{}^{0}/\sigma_{VV}{}^{0}$, dual-pol RVI, PRVI and DPSVI) for three representative canola fields at different growth stages. The in-situ measurements of Plant Area Index (PAI, $m^2 m^{-2}$), Vegetation water content (VWC, kg m^{-2}), and dry biomass (DB, kg m^{-2}) are plotted in third row for each field.

Analysis of canola is particularly interesting due to its dynamic morphological changes with phenology. Canola is a broad-leaf plant with distinctive differences in canopy structure throughout the growing season. Upon emergence, the plant develops a dense rosette of leaves near to the soil. Hence, the backscatter response is affected by the development of leaves, which have a similar size compared to the C-band wavelength ($\approx$5.6cm). The canola stem then bolts, increasing its vertical structure just before flowering and podding with an increase in both PAI and biomass (Wiseman et al., 2014). Latter in the pod development stage, canola forms a dense and complex canopy structure.

On 13 June, DpRVI is $\approx$0.35 in the majority of the canola fields, indicating low vegetation cover. In-situ measurements confirm that their growth was limited to the stem elongation stage with low PAI ($\approx$1.45 m^2 m^{-2}) and biomass (VWC = 1.0 kg m^{-2} and DB < 0.2 kg m^{-2}). The vegetation cluster in the $m - \beta$ polar plot (Fig. 8 shows a high value of $m \approx 0.90$ along with a high value of β ($\cos 20^{\circ} = 0.94$) during early development stages when canopy structure is less random. Similarly, a low value of $\sigma_{VH}{}^{0}/\sigma_{VV}{}^{0}$ and RVI also indicate sparse vegetation condition. Low values of the other two indices i.e., PRVI and DPSVI also indicative of low vegetation. Although the dynamic range of PRVI is low as compared to others, the increase in mean value throughout canola growth is observed.

In comparison to field 206 and 208, with low vegetation cover (i.e., PAI $\approx$ 0.5 $m^2 m^{-2}$) and VWC < 0.42 kg m^{-2}), a lower value of DpRVI ($\approx$0.18) is found in field 224, where the canola plants were still at their leaf development stage. At early growth stages, the backscattering is dominated by uncovered soil surface where a single dominant scattering mechanism is most apparent. This indicates that $\lambda_1 \gg \lambda_2$, and

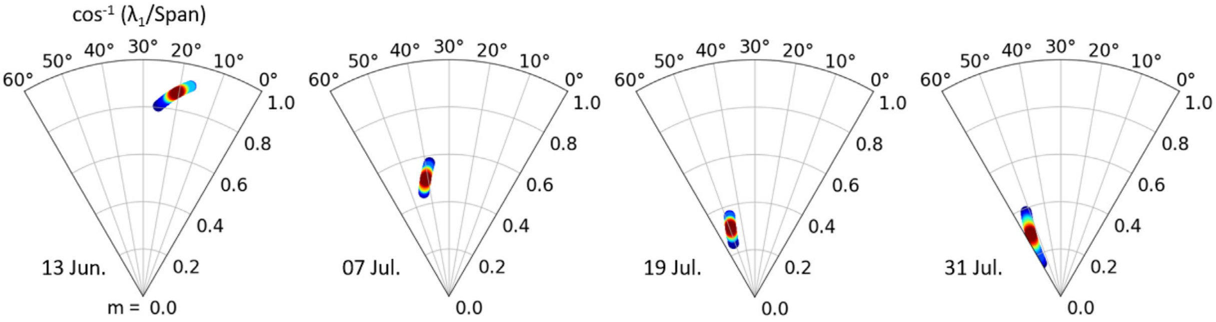

Fig. 8. Temporal variations of degree of polarization (m) and β in polar plots for canola fields.

consequently low DpRVI values.

The DpRVI values for each field increased rapidly as the plant growth progressed from the early vegetative stage to the beginning of pod development. During the early pod development stage (19 July), the DpRVI is ≈0.8 ± 0.04. At high growth stages, with the increase of vegetation elements, a decrease in m is likely due to the depolarization of incident waves from the complex vegetation canopy. During this pod development stage, the ramified stems and the randomly oriented pods create a complex upper canopy structure that may increase multiple scattering mechanisms. This aspect may lead to similar values of λ_1 and λ_2 (equal to Span/2). Variations in m and β with vegetation growth stages are apparent in Fig. 8. A significant increase in $\sigma_{VH}{}^0/\sigma_{VV}{}^0$ is observed during the inflorescence emergence and flowering stage, potentially due to changes in the cross-pol intensity as the canopy develops (Pacheco et al., 2016). Increment of PRVI with PAI is also apparent in the simulations presented by Chang et al. (2018), which indicate relatively linear relationships among LAI and PRVI.

During the advanced pod development to ripening stage, the DpRVI values are peculiarly confined within the range of 0.75 ± 0.05, rather than increasing from the early pod development stages. At the end of the pod development stage, in-situ measurements indicate high vegetation cover (PAI ≈ 6.0 $m^2\ m^{-2}$) and biomass (VWC > 3.0 kg m^{-2} and DB ≈ 1.0 kg m^{-2}). The sensitivity of the SAR signal to the accumulation of biomass from leaf development until the flowering stage is apparent in Fig. 7. Following this, a saturation of the C-band signal is likely due to the high volume of vegetation components during the pod development stage (Wiseman et al., 2014). Besides, the values of the other four indices also remain stable at high growth stages. These results are comparable to the backscatter response from canola reported in Veloso et al. (2017) and Vreugdenhil et al. (2018).

On 31 July, changes in all the five radar vegetation indices are less apparent with plant growth. Although the in-situ measurements were not available, the Manitoba agriculture weekly reports (Agriculture, 2016) indicates that the canola crops were at their pod development stage in this region. Hence, an increment in the order of scattering is expected as the crop canopy develops. Consequently, m is expected to decrease from early leaf development to pod development stage with $\lambda_1 \approx \lambda_2$. However, it can be noted that the incidence angle of Sentinel-1 data on 31 July is comparatively higher than other dates. At this high incidence angle (e.g., 39°), surface roughness and leaf layer have more contribution to scattering, which reduces the effect of volume contribution as the crop matures. Thus, the collective influence of changes in the incidence angle and crop growth renders the interpretation of radar vegetation indices challenging.

A quantitative assessment of vegetation indices is essential for comparative analysis. The correlation plots in Fig. 9 indicate that the DpRVI values are better correlated with the biophysical parameters of canola than the other four indices. It is observed that the coefficients of determination (R^2) for the PAI, VWC, and DB with DpRVI are 0.79, 0.82, and 0.75 respectively. Both $\sigma_{VH}{}^0/\sigma_{VV}{}^0$ and RVI produced lower correlations with PAI, VWC, and DB. Both $\sigma_{VH}{}^0/\sigma_{VV}{}^0$ and RVI produced higher correlations with crop biophysical parameters than PRVI and DPSVI. The DpRVI certainly outperforms these four vegetation indices both in terms of stronger correlations and lower variances throughout the entire growth stages.

4.2. Soybean

Unlike cereal and oil-seed crops, soybeans are legumes, which are characterized by more planophile canopy architecture. However, as soybeans mature, their canopy structure becomes more random due to its unique morphology with trifoliate leaves (a compound leaf made of three leaflets) attach to each stem node with petiole, secondary stems, and randomly oriented leaves (Fehr et al., 1971).

The Manitoba weekly crop reports (Agriculture, 2016) suggests that soybean seeding was completed by the 3rd week of May. Thus, crop development during the beginning of the SMAPVEX-16 campaign in June was primarily restricted to vegetative growth. Subsequently, inflorescence emergence, flowering, and pod initiation started during the last week of July. The development of pods, ripening of seeds, and senescence followed in August until the 2nd week of September.

Fig. 10 shows the temporal trends of the vegetation indices for three representative fields (Field no. 65, 72, and 232). It is evident from Fig. 10 that the DpRVI values for each field increase rapidly as the vegetation growth increases from the early leaf development stage to the beginning of pod development. The DpRVI value is ≈0.21 at the leaf development stage (on 13 June).

In-situ measurements confirm the vegetative growth with low PAI (≈0.35 $m^2\ m^{-2}$) and biomass (VWC = 0.2 kg m^{-2} and DB < 0.05 kg m^{-2}). The $m - \beta$ polar plot (Fig. 11 indicates that the vegetation cluster lies in the region of high m (≈0.90) and β during early development stages (i.e., 2nd trifoliate stage) with less random canopy structure. During this stage, the SAR backscatter is primarily affected by the underlying soil (Wang et al., 2016). It may be noted that a similar effect of soil on backscatter response at the early vegetative stage is also reported by Cable et al. (2014) with quad-pol RADARSAT-2 SAR data. Alongside, low values of $\sigma_{VH}{}^0/\sigma_{VV}{}^0$ and RVI also indicate an early stage of vegetation growth. Furthermore, low values of PRVI and DPSVI are similarly aligned with the crop condition. However, Veloso et al. (2017) reported a higher standard deviation of the co-pol channel than cross-pol for bare soil conditions, which may impart bias in $\sigma_{VH}{}^0/\sigma_{VV}{}^0$ and RVI values.

With the increase in vegetation components, the variations in DpRVI values among several fields are apparent. The DpRVI reaches its highest value (≈0.55) at the end of the flowering stage when the volume scattering component increases. Moreover, biophysical parameters also peak (PAI > 3.0 $m^2\ m^{-2}$, VWC > 1.25 kg m^{-2}, and DB 0.40 kg m^{-2}) during this stage. Wigneron et al. (2004) indicated random scattering behaviour at high vegetative growth of soybean rather than a dominant scattering component. A significant increase in $\cos^{-1}\beta$ along with a decrease in m at peak growth stage (Fig. 11 is in agreement with these findings. Conversely, variations in $\sigma_{VH}{}^0/\sigma_{VV}{}^0$ and RVI values are higher than DpRVI, which is likely due to lower attenuation of the co-pol channel at pod development stages. Similar to canola, we can observe a low dynamic range of DPSVI throughout the growth stages of soybean. Conversely, the PRVI mimics the trends of the crop biophysical parameters.

The correlation plots in Fig. 12 indicate that DpRVI values are better correlated with the biophysical parameters than $\sigma_{VH}{}^0/\sigma_{VV}{}^0$, dual-pol RVI, PRVI, and DPSVI. The coefficients of determination (R^2) for PAI, VWC, and DB with DpRVI are 0.58, 0.55, and 0.57, respectively. Even though the correlations are statistically significant, the R^2 values are lower than that of canola (Fig. 9). It is likely that the indices derived for low biomass canopies are significantly influenced by scattering from the underlying soil rather than the vegetation canopy. This effect is more apparent for PRVI and DPSVI with higher dispersion of the estimates.

4.3. Wheat

Wheat belongs to the graminaceous plant family, which is characterized by erectophile (canopy elements have predominant vertical distribution) architecture. This morphological diversity leads to distinctive backscatter responses and associated vegetation indices. In the test site, wheat was sown at the beginning of May. Most fields were at the tillering stage on 13 June and then advanced to the heading stage by the end of June. Flowering and fruit development started mid-July, with the onset of dough and maturity stages at the end of July. The corresponding vegetation indices derived from time-series Sentinel-1 data are shown in Fig. 13.

Variations in DpRVI values among three representative fields (Field no. 220, 233, and 62) are evident with vegetation growth. Lowest

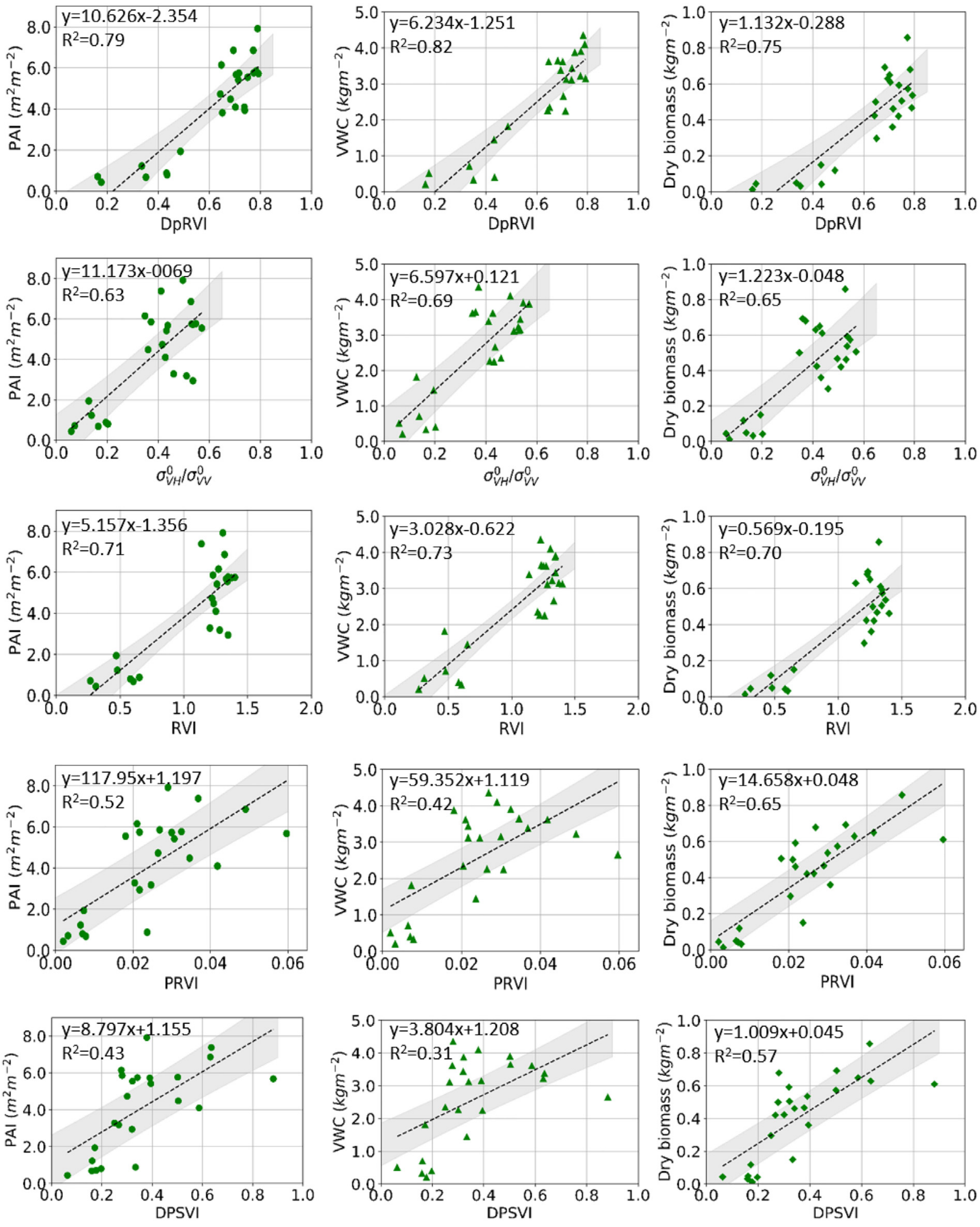

Fig. 9. Correlation analysis between vegetation indices (DpRVI, $\sigma_{VH}{}^0/\sigma_{VV}{}^0$ and RVI) and crop biophysical parameters, i.e., Plant Area Index (PAI, m^2 m^{-2}), Vegetation water content (VWC, kg m m^{-2}), and dry biomass (DB, kg m m^{-2}) for canola. The linear regression line is indicated as black dashed line. The 95% confidence limits are highlighted as gray regions.

DpRVI values are observed when wheat advanced from the leaf development to the tillering stage on 13 June. Fields with plant density (PD) of ≈ 100 m^{-2} (Fields no. 220) have low DpRVI values (≈ 0.22), which are comparatively lower than wheat fields (Field no. 233 and 62) with high PD (125 m^{-2} and 190 m^{-2}). In-situ measurements of PAI and VWC are also relatively higher (> 2.5 m^2m^{-2} and ≈ 1.1 kg m^{-2}) for wheat fields with high plant density. In comparison to other crops, wheat gained more vegetative components on 13 June (apparent in their high biophysical parameter values), which lead to higher DpRVI values. The $m - \beta$ polar plot (Fig. 14) also indicates moderate to high values of m (≈ 0.65) and β (cos35 ° $= 0.82$) on 13 June.

The DpRVI values reached its maximum when the crop advanced from flowering to early dough stages on 19 July. DpRVI reaches up to 0.74 for low PD fields (Field no. 220), while these values peak at ≈ 0.8

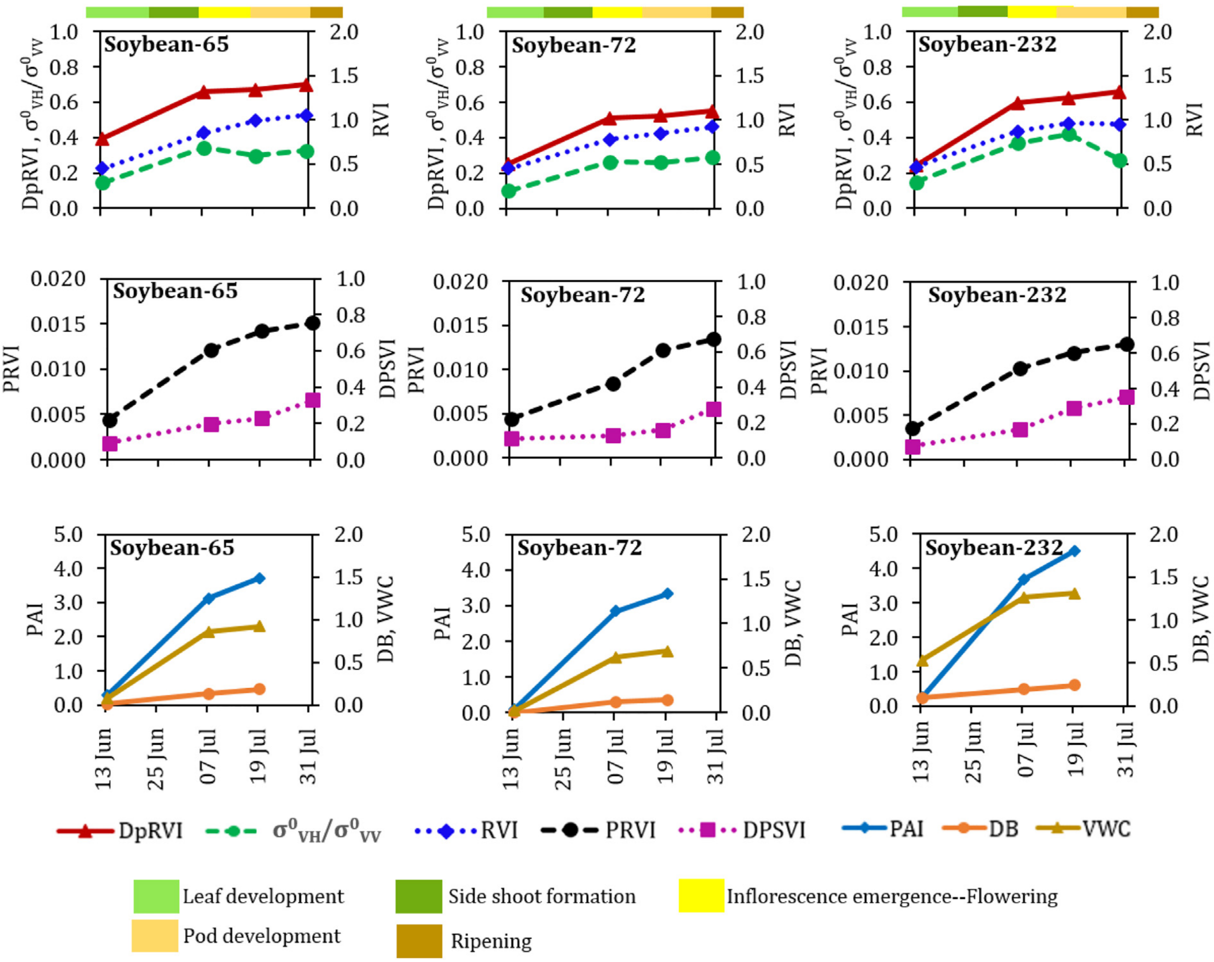

Fig. 10. Temporal pattern of vegetation indices (DpRVI, $\sigma_{VH}{}^{0}/\sigma_{VV}{}^{0}$, dual-pol RVI, PRVI and DPSVI) for three representative soybean fields at different growth stages. The in-situ measurements of Plant Area Index (PAI, $m^2\ m^{-2}$), Vegetation water content (VWC, $kg\ m^{-2}$), and dry biomass (DB, $kg\ m^{-2}$) are plotted in second row for each field.

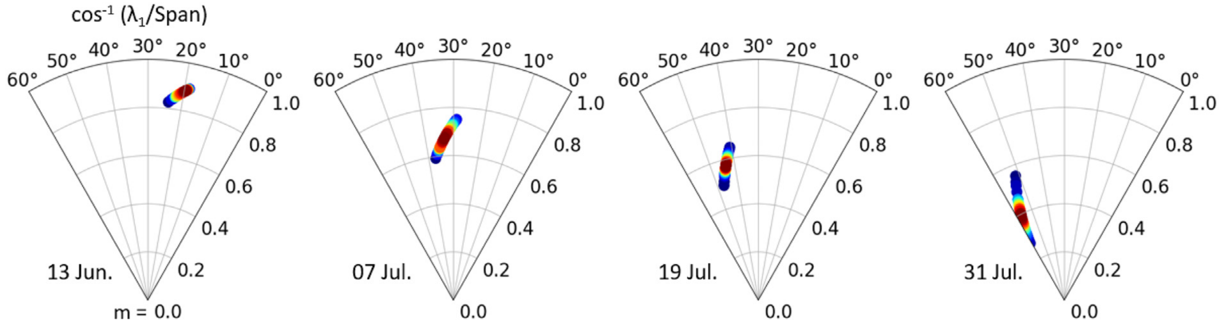

Fig. 11. Temporal variations of degree of polarization (m) and β in polar plots for soybean fields.

for fields with high PD (Field no. 233 and 62). This difference may be due to the high degree of randomness in scattering ($m \approx 0.35$ and $\cos^{-1}\beta \approx 50^{\circ} - 55^{\circ}$ on 19 July) from the canopy elements during the flowering to fruit development stages. In-situ measurements of plant biophysical parameters at these stages confirm their increment up to approximately 6.2 to 8.1 $m^2\ m^{-2}$, 3.0 $kg\ m^{-2}$, and 1.1 $kg\ m^{-2}$, for PAI, VWC, and DB, respectively. Significant contributions due to multiple scattering from the canopy might lead to $\lambda_1 \approx \lambda_2 \approx$ Span/2 (i.e., no dominant scattering) with low values of m ($\approx$0.25).

The differential increase in DpRVI values among the wheat fields is visible in Fig. 13. Variations in plant density might cause a difference in DpRVI values among several fields, even though all fields are in the same phenological stage. The rate of increase in DpRVI slows down at the end of July after the stagnation of vegetative growth and the onset of seed development. Similarly, the values of $\sigma_{VH}{}^{0}/\sigma_{VV}{}^{0}$ and RVI follow the vegetation growth trends of wheat. $\sigma_{VH}{}^{0}/\sigma_{VV}{}^{0}$ increases during heading to flowering as the plant biomass accumulates. Similar results are also reported by Veloso et al. (2017) for cereal crops during these phenology stages. The temporal trends of dual-pol RVI, PRVI and DPSVI are also inline with plant growth.

The correlation analysis of vegetation indices with plant biophysical parameters is provided in Fig. 15. The R^2 of DpRVI with PAI, VWC, and DB are 0.62, 0.62, and 0.57, respectively, which are higher than the R^2 of $\sigma_{VH}{}^{0}/\sigma_{VV}{}^{0}$, dual-pol RVI, PRVI, and DPSVI. The dispersion of DpRVI

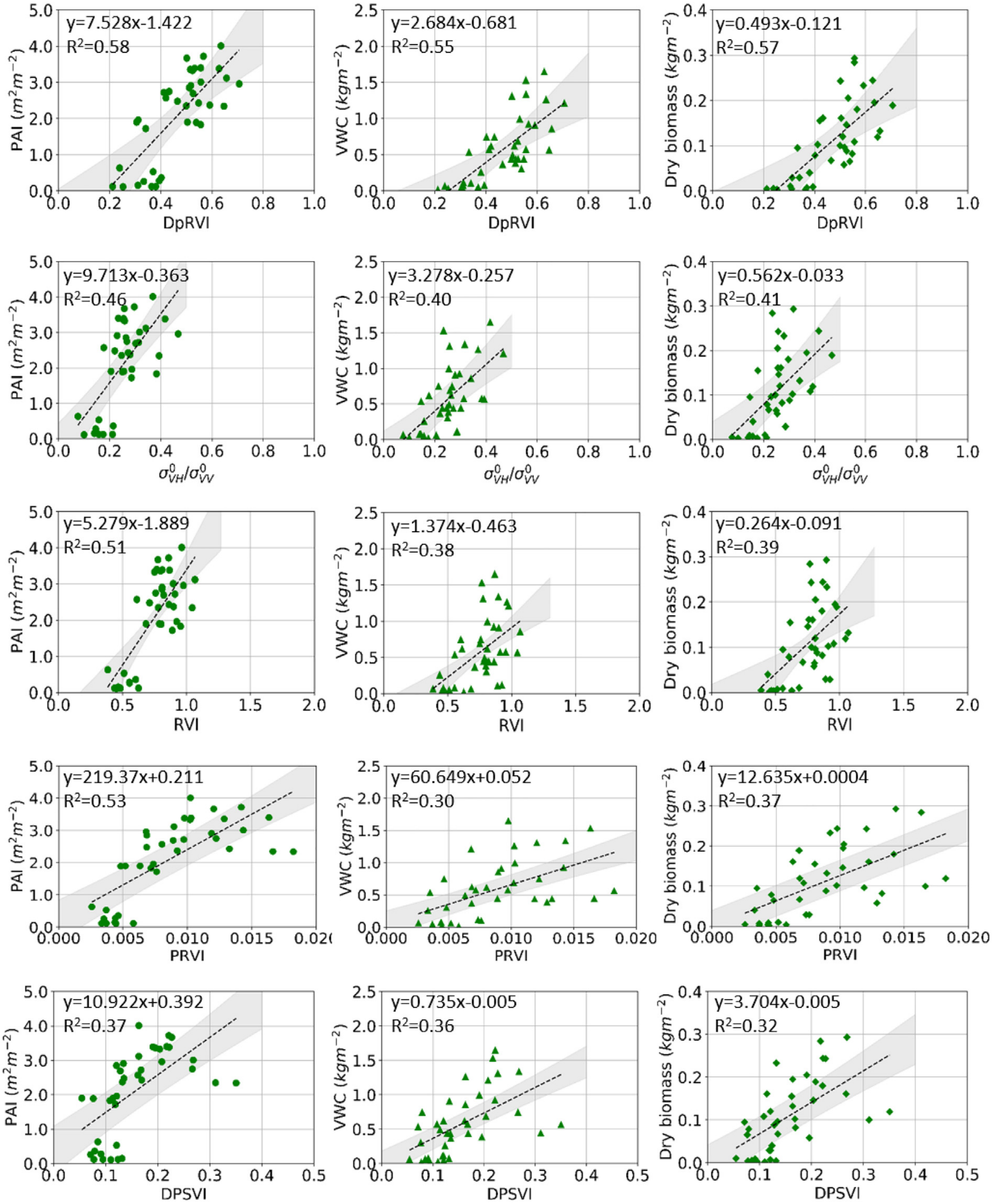

Fig. 12. Correlation analysis between vegetation indices (DpRVI, $\sigma_{VH}{}^{0}/\sigma_{VV}{}^{0}$, dual-pol RVI, PRVI and DPSVI) and crop biophysical parameters, i.e., Plant Area Index (PAI, $m^2\ m^{-2}$), Vegetation water content (VWC, $kg\ m^{-2}$), and dry biomass (DB, $kg\ m^{-2}$) for soybean. The linear regression line is indicated as black dashed line. The 95% confidence limits are highlighted as gray regions.

values in the correlation plot at later growth stages is likely due to scattering from the upper canopy layer (i.e., wheat heads). Wu et al. (1985) reported similar results stating that the wheat heads dominate the total scattering power at the heading stage. However, during the ripening stage (when the heads become drier), the backscatter from the ground dominants, and the backscatter power from the heads is insensitive to the moisture content. Furthermore, variations in backscatter power are less prominent with changes in the leaf area or biomass (Jia et al., 2013).

4.4. Crop biophysical parameter retrieval

The retrieval of biophysical parameters from SAR observations is of vital importance for in-season monitoring of crop growth. The PAI, VWC and dry biomass are valuable indicators of crop condition. Considering the highest correlations among DpRVI and the three

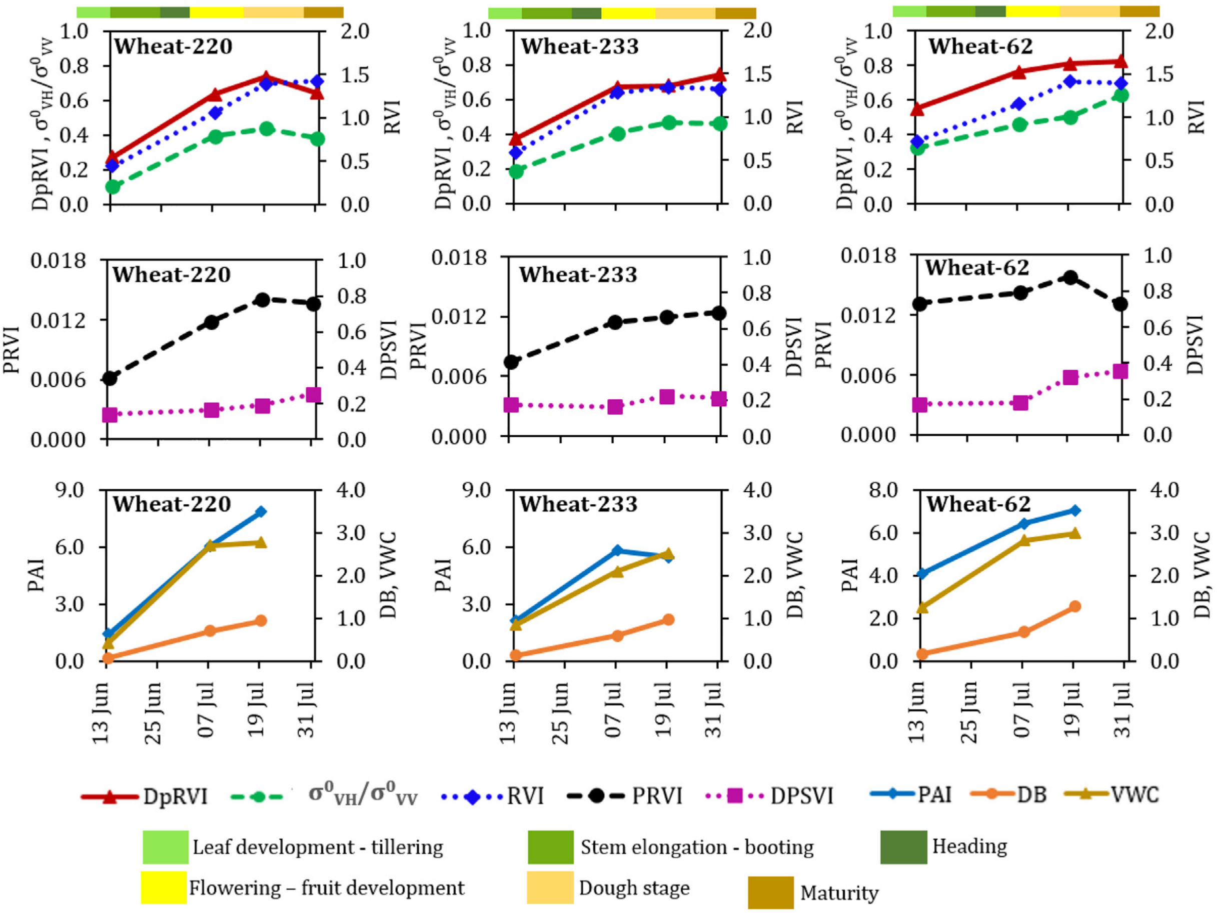

Fig. 13. Temporal pattern of vegetation indices (DpRVI, $\sigma_{VH}{}^0/\sigma_{VV}{}^0$, dual-pol RVI, PRVI and DPSVI) for three representative wheat fields at different growth stages. The in-situ measurements of Plant Area Index (PAI, $m^2\ m^{-2}$), Vegetation water content (VWC, kg m^{-2}), and dry biomass (DB, kg m^{-2}) are plotted in second row for each field.

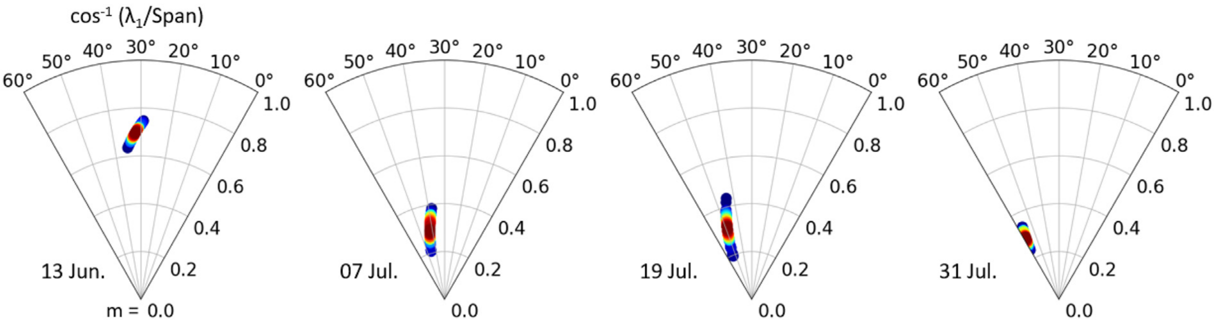

Fig. 14. Temporal variations of degree of polarization (m) and β in polar plots for wheat fields.

biophysical parameters for canola, soybean and wheat (Figs. 9, 12, 15), linear regression models are adopted for biophysical parameter estimation. A k-fold (k = 5 in this case) cross-validation is performed while estimating biophysical parameters using DpRVI. We measure the retrieval accuracy in terms of coefficient of determination (R^2), Root Mean Square Error (RMSE) and Mean Absolute Error (MAE) with each validation datasets. Among them, the best result is considered for representation, as shown in Table 2.

The PAI estimation for canola showed high R^2 with RMSE = 1.028 $m^2.m^{-2}$ and MAE = 0.844 $m^2.m^{-2}$. VWC and DB estimates also exhibit high correlation (R^2 = 0.83 and 0.75) with in-situ measurements. Lower error rates for VWC (RMSE = 0.527 kg m^{-2} and MAE = 0.451 kg m^{-2}) and DB (RMSE = 0.124 kg m^{-2} and MAE = 0.106 kg m^{-2}) are also within admissible range. The error estimates of soybean and wheat are also consistent with the reported errors in previous studies (Mandal et al., 2019, 2020a). The ranges of biophysical parameters for specific acquisition dates for each crop can be observed in the biophysical parameter maps, shown in Fig. 16.

Using DpRVI from Sentinel-1 image acquired on 13 June, 07 July, and 19 July, we produce PAI, VWC and DB maps (20 m resolution) respectively using the regression models developed for canola, soybeans and wheat (Fig. 16). The land cover map (adapted from the annual crop inventory map prepared by Agriculture and Agri-Food Canada (AAFC) (Davidson et al., 2017)) over the test site allowed the selective application of the models developed for a specific crop pertaining only in that particular crop fields. In the absence of any regression model for corn and oats, we masked out these fields in this study. Both spatial, as well as temporal variability in crop growth, are

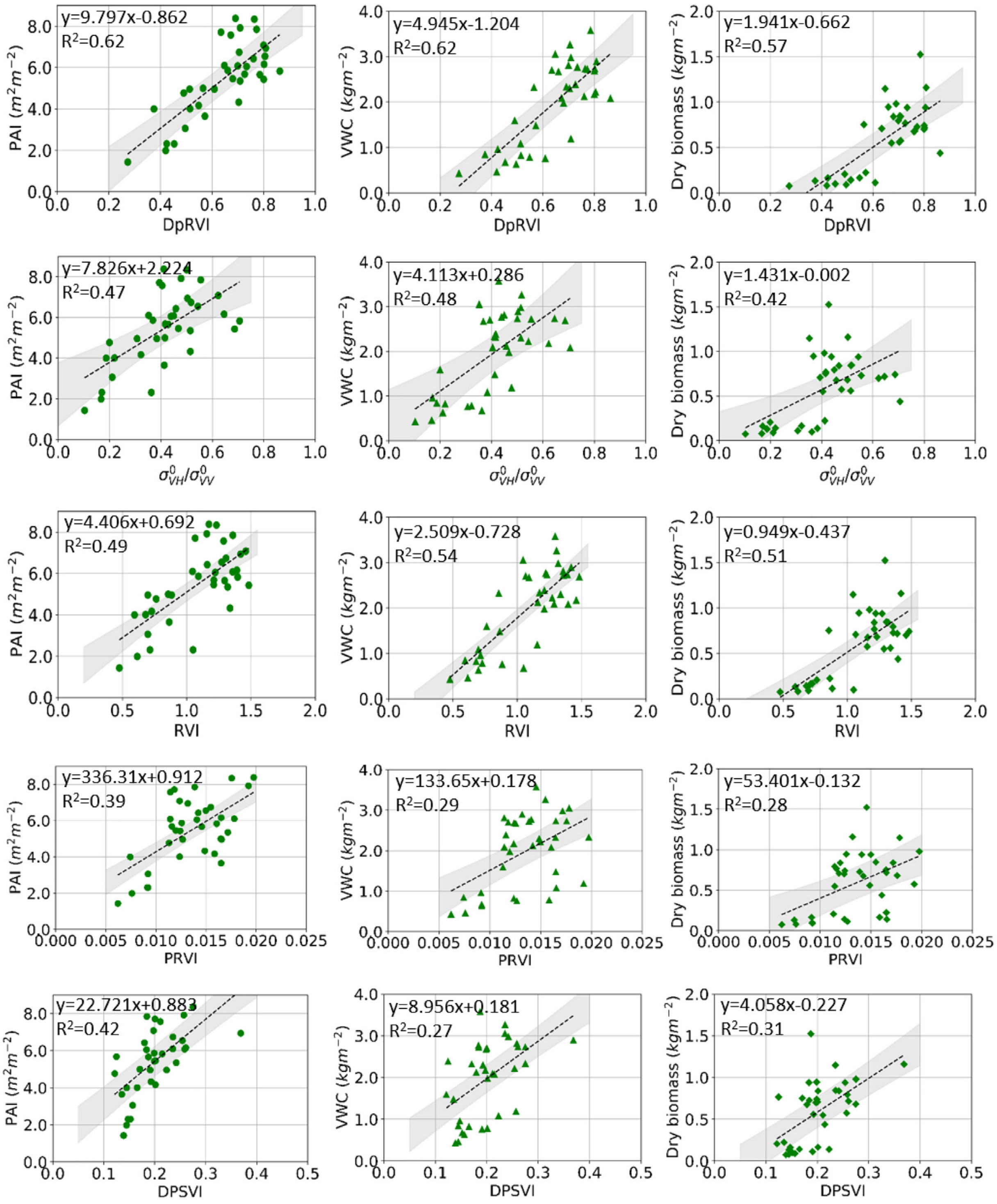

Fig. 15. Correlation analysis between vegetation indices (DpRVI, $\sigma_{VH}{}^0/\sigma_{VV}{}^0$, dual-pol RVI, PRVI and DPSVI) and crop biophysical parameters, i.e., Plant Area Index (PAI, $m^2\ m^{-2}$), Vegetation water content (VWC, kg m^{-2}), and dry biomass (DB, kg m^{-2}) for wheat. The linear regression line is indicated as black dashed line. The 95% confidence limits are highlighted as gray regions.

observed for various fields in these map products.

On 13 June, the estimated PAI in majority of canola and soybean fields are low (about 1.0 $m^2\ m^{-2}$and 0.5 $m^2\ m^{-2}$) as compared to wheat fields. The VWC and DB maps on 13 June are also indicative of these variations between crop fields. Increases in PAI, VWC and DB are observed in Fig. 16 up to 5.0 $m^2\ m^{-2}$, 2.5 $m^2\ m^{-2}$ and 0.75 kg m^{-2}, respectively for canola on 07 July. A rapid increase in biophysical parameters is apparent for the wheat fields. During the first week of July, good crop growth was also reported in the Manitoba weekly crop reports (Agriculture, 2016). In contrast, for soybean, increases in VWC and DB are negligible as can be seen in the map products. During the third week of July, most crops were at the end of their vegetative growth stage and the commencement of their reproductive stages. Hence, the increase in biophysical parameters for all crops is apparent on 19 July. It is interesting to note the rapid growth in soybean fields as evident on 19 July as soybeans continue to flower at the end of the vegetative stage.

Table 2
Validation accuracies for crop biophysical parameter retrieval using DpRVI. The error estimates are presented in terms of coefficient of determination (R^2), Root Mean Square Error (RMSE) and Mean Absolute Error (MAE).

Crop	Parameter	Regression model	Validation accuracy		
			R^2	RMSE	MAE
Canola	PAI	10.626 × DpRVI − 2.354	0.79	1.028	0.844
	VWC	6.234 × DpRVI − 1.251	0.83	0.527	0.451
	DB	1.132 × DpRVI − 0.288	0.75	0.124	0.106
Soybean	PAI	7.528 × DpRVI − 1.422	0.576	0.795	0.705
	VWC	2.684 × DpRVI − 0.681	0.545	0.302	0.243
	DB	0.493 × DpRVI − 0.121	0.526	0.057	0.046
Wheat	PAI	9.797 × DpRVI − 0.862	0.61	1.115	0.904
	VWC	4.945 × DpRVI − 1.204	0.56	0.561	0.447
	DB	1.941 × DpRVI − 0.662	0.55	0.248	0.201

5. Conclusion

We have proposed a dual-pol radar vegetation index (DpRVI) for Sentinel-1 (VV-VH) SAR data. The index is derived using the degree of polarization (m) and the dominant normalized eigenvalue ($\beta = \lambda_1/\text{Span}$) obtained from the 2 × 2 covariance matrix. The DpRVI is assessed for three crop types (canola, soybean, and wheat) to characterize vegetation growth throughout the phenology of these crops. The DpRVI followed the advancement of plant growth until full canopy development with the accumulation of the Plant Area Index (PAI) and biomass (vegetation water content (VWC) and dry biomass (DB)). Strong and moderate correlations are reported between DpRVI and these biophysical parameters.

Among the results obtained from three different crops, canola delivered the highest correlation (R^2) with its biophysical parameters: 0.79 (PAI), 0.82 (VWC), and 0.75 (DB). In contrast, DpRVI showed moderate correlations with biophysical parameters of wheat and

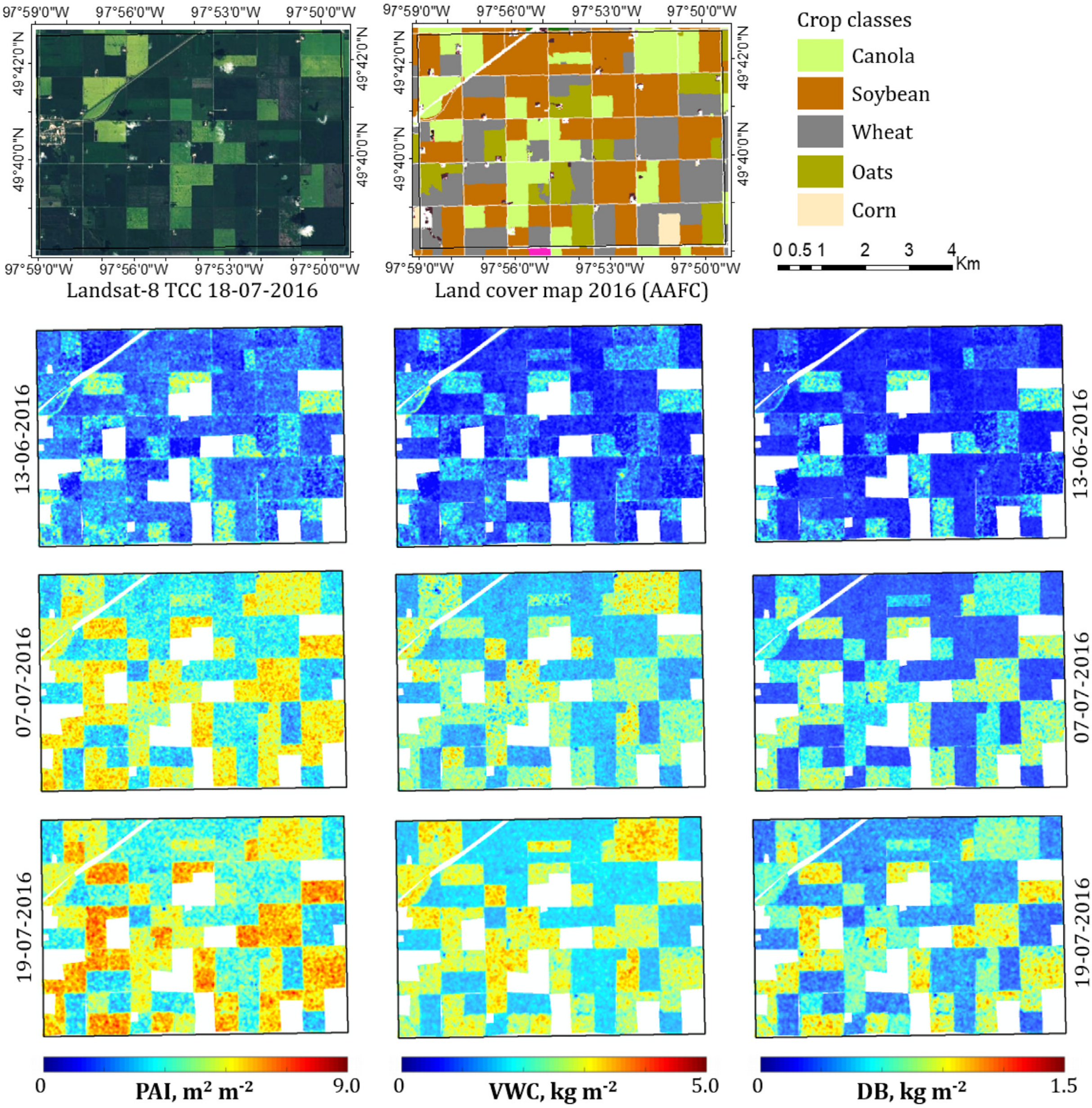

Fig. 16. Plant Area Index (PAI $\text{m}^2\ \text{m}^{-2}$), Vegetation Water Content (VWC, kg m^{-2}), and Dry Biomass (DB, kg m^{-2}) maps over the test site for three acquisitions dates (13-06-2016, 07-07-2016, and 19-07-2016). The land cover map (produced by AAFC) and Landsat-8 True Colour Composite (TCC) image (acquired on 18-07-2016) over the subset area are highlighted.

soybean. It is noted that the correlations of DpRVI are comparatively better than that of ${\sigma_{VH}}^0/{\sigma_{VV}}^0$, dual-pol RVI, PRVI, and DPSVI for all crops. Rather than using the polarization channel backscatter intensities, the DpRVI exploits the normalized dominant eigenvalue and the degree of polarization, which are roll and polarization basis invariant. It can be concluded that the DpRVI effectively incorporates the scattered wave information to describe the phenological changes that are vital for time-series crop monitoring. Moreover, the crop biophysical parameters are accurately retrieved using linear regression models with DpRVI.

Notably, the proposed DpRVI for dual-pol SAR data holds significant interest from an operational perspective for the Sentinel-1 Copernicus mission, the RADARSAT Constellation Mission (RCM) and other upcoming SAR missions, such as NISAR. These missions provide data across larger spatial extents with short revisit time. For example, end-users might be interested in weekly vegetation condition products from an operational mission like Sentinel-1, particularly in regions where cloud cover obscures the Earth to optical satellite acquisitions.

With the synergy of Sentinel-1A and 1B, monitoring crop conditions every 6 days is possible at national scales with dual-pol indices would be an adequate proxy. However, further assessment of the HH-HV mode is required, as crop response could be different for horizontally polarized transmitted wave relative to vertically transmitted. Moreover, experimental validation of vegetation indices on the incidence angle variations is necessary for wide swath products. Finally, the vegetation index needs to be further investigated for different cropping systems at various test sites. This investigation is planned for dense time-series data cubes which have been acquired under the JECAM SAR Inter-Comparison Experiment.

Disclosures

No potential conflict of interest is reported by the authors.

Acknowledgment

The authors would like to thank the ground team members for data collection through the SMAPVEX16-MB campaign, and the European Space Agency (ESA) for providing Sentinel-1 through Copernicus Open Access Hub. Authors acknowledge the GEO-AWS Earth Observation Cloud Credits Program, which supported the computation on AWS cloud platform through the project “AWS4AgriSAR-Crop inventory mapping from SAR data on cloud computing platform”. This work was supported by the Spanish Ministry of Science, Innovation and Universities, the State Agency of Research (AEI) and the European Funds for Regional Development (EFRD) under Project TEC2017-85244-C2-1-P.

Appendix A. Relationship between *m* and *β*

The eigen-decomposition of a 2 × 2 covariance matrix, $\mathbf{C}_2$ can be expressed as,

$$\mathbf{C}_2 = \mathbf{U}_2\mathrm{S}\mathbf{U}_2^{-1} \tag{A.1}$$

where,

$$\Sigma = \begin{bmatrix} \lambda_1 & 0 \\ 0 & \lambda_2 \end{bmatrix} \tag{A.2}$$

is a 2 × 2 diagonal matrix with non-negetive elements, $\lambda_1 \geq \lambda_2 \geq 0$, which are the eigenvalues of the covariance matrix, and $\mathbf{U}_2$ is a 2 × 2 unitary matrix whose columns are the eigenvectors of the covariance matrix.

The degree of polarization (m) of the EM wave is derived from the expression given by Barakat (1977) as,

$$m = \sqrt{1 - \frac{4|\mathbf{C}_2|}{(\mathrm{Tr}(\mathbf{C}_2))^2}} \tag{A.3}$$

It can be noted that m can also be expressed in terms of the eigenvalues as,

$$m = \sqrt{\left[1 - \frac{4\lambda_1\lambda_2}{(\lambda_1 + \lambda_2)^2}\right]} = \sqrt{\left[\frac{(\lambda_1 + \lambda_2)^2 - 4\lambda_1\lambda_2}{(\lambda_1 + \lambda_2)^2}\right]} = \frac{\lambda_1 - \lambda_2}{\lambda_1 + \lambda_2} \tag{A.4}$$

The normalized dominant eigenvalue, β is given as, $\lambda_1/\mathrm{Span} = \lambda_1/(\lambda_1 + \lambda_2)$. Hence, the differential variation between m and β is expressed as, $\beta - m = \lambda_2/(\lambda_1 + \lambda_2) = \lambda_2/\mathrm{Span}$.

References

Agriculture, M.B., 2016. Agriculture Province of Manitoba. URL. http://www.gov.mb.ca/agriculture/crops/seasonal-reports/crop-report-archive/index.html.

Ainsworth, T., Kelly, J., Lee, J.-S., 2009. Classification comparisons between dual-pol, compact polarimetric and quad-pol SAR imagery. ISPRS J. Photogramm. Remote Sens. 64 (5), 464–471.

Arias, M., Campo-Bescos, M.A., Alvarez-Mozos, J., 2020. Crop classification based on temporal signatures of Sentinel-1 observations over Navarre province, Spain. Remote Sens. 12 (2) URL. https://www.mdpi.com/2072-4292/12/2/278.

Barakat, R., 1977. Degree of polarization and the principal idempotents of the coherency matrix. Opt. Commun. 23 (2), 147–150.

Bargiel, D., 2017. A new method for crop classification combining time series of radar images and crop phenology information. Remote Sens. Environ. 198, 369–383.

Bhuiyan, H.A., McNairn, H., Powers, J., Friesen, M., Pacheco, A., Jackson, T.J., Cosh, M.H., Colliander, A., Berg, A., Rowlandson, T., et al., 2018. Assessing SMAP soil moisture scaling and retrieval in the carman (Canada) study site. Vadose Zone J. 17 (1).

Blaes, X., Defourny, P., Wegmuller, U., Della Vecchia, A., Guerriero, L., Ferrazzoli, P., 2006. C-band polarimetric indexes for maize monitoring based on a validated radiative transfer model. IEEE Trans. Geosci. Remote Sens. 44 (4), 791–800.

Boryan, C., Yang, Z., Mueller, R., Craig, M., 2011. Monitoring US agriculture: the US department of agriculture, national agricultural statistics service, cropland data layer program. Geocarto Int. 26 (5), 341–358.

Bousbih, S., Zribi, M., Lili-Chabaane, Z., Baghdadi, N., El Hajj, M., Gao, Q., Mougenot, B., 2017. Potential of Sentinel-1 radar data for the assessment of soil and cereal cover parameters. Sensors 17 (11), 2617.

Cable, J., Kovacs, J., Jiao, X., Shang, J., 2014. Agricultural monitoring in northeastern Ontario, Canada, using multi-temporal polarimetric RADARSAT-2 data. Remote Sens. 6 (3), 2343–2371.

Canisius, F., Shang, J., Liu, J., Huang, X., Ma, B., Jiao, X., Geng, X., Kovacs, J.M., Walters, D., 2018. Tracking crop phenological development using multi-temporal polarimetric Radarsat-2 data. Remote Sens. Environ. 210, 508–518.

Chang, J., Shoshany, M., 2017. Radar polarization and ecological pattern properties across Mediterranean-to-arid transition zone. Remote Sens. Environ. 200, 368–377.

Chang, J.G., Shoshany, M., Oh, Y., 2018. Polarimetric radar vegetation index for biomass estimation in desert fringe ecosystems. IEEE Trans. Geosci. Remote Sens. 56 (12), 7102–7108.

Chipanshi, A., Zhang, Y., Kouadio, L., Newlands, N., Davidson, A., Hill, H., Warren, R., Qian, B., Daneshfar, B., Bedard, F., et al., 2015. Evaluation of the Integrated Canadian Crop Yield Forecaster (ICCYF) model for in-season prediction of crop yield across the Canadian agricultural landscape. Agric. For. Meteorol. 206, 137–150.

Davidson, A., Fisette, T., Mcnairn, H., Daneshfar, B., 2017. Detailed crop mapping using remote sensing data (crop data layers). In: Delincé, J. (Ed.), Handbook on Remote Sensing for Agricultural Statistics. Global Strategy to improve Agricultural and Rural Statistics (GSARS), Rome, pp. 91–129 Ch. 4.

De Bernardis, C.G., Vicente-Guijalba, F., Martinez-Marin, T., Lopez-Sanchez, J.M., March 2015. Estimation of key dates and stages in rice crops using dual-polarization SAR time series and a particle filtering approach. IEEE J. Select. Topics Appl. Earth Observ. Rem. Sens. 8 (3), 1008–1018.

Denize, J., Hubert-Moy, L., Betbeder, J., Corgne, S., Baudry, J., Pottier, E., 2019. Evaluation of using Sentinel-1 and-2 time-series to identify winter land use in agricultural landscapes. Remote Sens. 11 (1), 37.

ESA, 2015. User Guides - Sentinel-1 SAR. URL. https://sentinel.esa.int/web/sentinel/user-guides/sentinel-1-sar/acquisition-modes/interferometric-wide-swath.

ESA, 2017. Sen4CAP - Sentinels for Common Agriculture Policy. URL. `http://esa-sen4cap.org/`.

Fehr, W., Caviness, C., Burmood, D., Pennington, J., 1971. Stage of development descriptions for soybeans, Glycine Max (L.) Merrill 1. Crop Sci. 11 (6), 929–931.

Fikriyah, V.N., Darvishzadeh, R., Laborte, A., Khan, N.I., Nelson, A., 2019. Discriminating transplanted and direct seeded rice using Sentinel-1 intensity data. Int. J. Appl. Earth Obs. Geoinf. 76, 143–153.

Gururaj, P., Umesh, P., Shetty, A., 2019. Assessment of spatial variation of soil moisture during maize growth cycle using SAR observations. In: Remote Sensing for Agriculture, Ecosystems, and Hydrology XXI. 11149. International Society for Optics and Photonics, pp. 1114916.

Inglada, J., Vincent, A., Arias, M., Marais-Sicre, C., 2016. Improved early crop type identification by joint use of high temporal resolution SAR and optical image time series. Remote Sens. 8 (5), 362.

Jia, M., Tong, L., Zhang, Y., Chen, Y., 2013. Multitemporal radar backscattering measurement of wheat fields using multifrequency (L, S, C, and X) and full-polarization. Radio Sci. 48 (5), 471–481.

Khabbazan, S., Vermunt, P., Steele-Dunne, S., Ratering Arntz, L., Marinetti, C., van der Valk, D., Iannini, L., Molijn, R., Westerdijk, K., van der Sande, C., 2019. Crop monitoring using Sentinel-1 data: a case study from the Netherlands. Remote Sens. 11 (16), 1887.

Kim, Y., van Zyl, J.J., 2009. A time-series approach to estimate soil moisture using polarimetric radar data. IEEE Trans. Geosci. Remote Sens. 47 (8), 2519–2527.

Kumar, P., Prasad, R., Gupta, D., Mishra, V., Vishwakarma, A., Yadav, V., Bala, R., Choudhary, A., Avtar, R., 2018. Estimation of winter wheat crop growth parameters using time series Sentinel-1A SAR data. Geocarto Int. 33 (9), 942–956.

Kussul, N., Lemoine, G., Gallego, F.J., Skakun, S.V., Lavreniuk, M., Shelestov, A.Y., 2016. Parcel-based crop classification in Ukraine using Landsat-8 data and Sentinel-1A data. IEEE J. Select. Topics Appl. Earth Observ. Rem. Sens. 9 (6), 2500–2508.

Lasko, K., Vadrevu, K.P., Tran, V.T., Justice, C., 2018. Mapping double and single crop paddy rice with Sentinel-1A at varying spatial scales and polarizations in Hanoi, Vietnam. IEEEJ. Select. Topics Appl. Earth Observ. Rem. Sens. 11 (2), 498–512.

Lee, J.-S., Grunes, M.R., Pottier, E., 2001. Quantitative comparison of classification capability: fully polarimetric versus dual and single-polarization sar. IEEE Trans. Geosci. Remote Sens. 39 (11), 2343–2351.

López-Lozano, R., Duveiller, G., Seguini, L., Meroni, M., Garca-Condado, S., Hooker, J., Leo, O., Baruth, B., 2015. Towards regional grain yield forecasting with 1 km-resolution EO biophysical products: strengths and limitations at pan-European level. Agric. For. Meteorol. 206, 12–32.

Lopez-Sanchez, J.M., Vicente-Guijalba, F., Ballester-Berman, J.D., Cloude, S.R., May 2014. Polarimetric response of rice fields at C-band: analysis and phenology retrieval. IEEE Trans. Geosci. Remote Sens. 52 (5), 2977–2993.

Mandal, D., Kumar, V., Bhattacharya, A., Rao, Y.S., Siqueira, P., Bera, S., 2018. Sen4Rice: a processing chain for differentiating early and late transplanted rice using time-series Sentinel-1 SAR data with Google Earth engine. IEEE Geosci. Remote Sens. Lett. 15 (12), 1947–1951.

Mandal, D., Kumar, V., McNairn, H., Bhattacharya, A., Rao, Y., 2019. Joint estimation of Plant Area Index (PAI) and wet biomass in wheat and soybean from C-band polarimetric SAR data. Int. J. Appl. Earth Obs. Geoinf. 79, 24–34.

Mandal, D., Kumar, V., Lopez-Sanchez, J.M., Bhattacharya, A., McNairn, H., Rao, Y., 2020a. Crop biophysical parameter retrieval from Sentinel-1 SAR data with a multi-target inversion of Water Cloud Model. Int. J. Remote Sens. 41 (14), 5503–5524.

Mandal, D., Kumar, V., Ratha, D., Lopez-Sanchez, J.M., Bhattacharya, A., McNairn, H., Rao, Y., Ramana, K., 2020b. Assessment of rice growth conditions in a semi-arid region of India using the Generalized Radar Vegetation Index derived from RADARSAT-2 polarimetric SAR data. Remote Sens. Environ. 237, 111561.

Mandal, D., Ratha, D., Bhattacharya, A., Kumar, V., McNairn, H., Rao, Y.S., Frery, A.C., 2020c. A radar vegetation index for crop monitoring using compact polarimetric sar data. IEEE Trans. Geosci. Rem. Sens. https://doi.org/10.1109/TGRS.2020.2976661.

McNairn, H., Shang, J., 2016. A review of multitemporal synthetic aperture radar (SAR) for crop monitoring. In: Multitemporal Remote Sensing. Springer, pp. 317–340.

McNairn, H., Champagne, C., Shang, J., Holmstrom, D., Reichert, G., 2009. Integration of optical and Synthetic Aperture Radar (SAR) imagery for delivering operational annual crop inventories. ISPRS J. Photogramm. Remote Sens. 64 (5), 434–449.

McNairn, H., Tom, J.J., Powers, J., BÃlair, S., Berg, A., Bullock, P., Colliander, A., Cosh, M.H., Kim, S.-B., Ramata, M., Pacheco, A., Merzouki, A., 2016. Experimental Plan SMAP Validation Experiment 2016 in Manitoba, Canada (SMAPVEX16-MB). URL. `https://smap.jpl.nasa.gov/internal_resources/390/`.

McNairn, H., Jiao, X., Pacheco, A., Sinha, A., Tan, W., Li, Y., 2018. Estimating canola phenology using synthetic aperture radar. Remote Sens. Environ. 219, 196–205.

Nasirzadehdizaji, R., Balik Sanli, F., Abdikan, S., Cakir, Z., Sekertekin, A., Ustuner, M., 2019. Sensitivity analysis of multi-temporal sentinel-1 SAR parameters to crop height and canopy coverage. Appl. Sci. 9 (4), 655.

Nelson, A., Setiyono, T., Rala, A., Quicho, E., Raviz, J., Abonete, P., Maunahan, A., Garcia, C., Bhatti, H., Villano, L., et al., 2014. Towards an operational SAR-based rice monitoring system in Asia: examples from 13 demonstration sites across Asia in the RIICE project. Remote Sens. 6 (11), 10773–10812.

Nguyen, D.B., Gruber, A., Wagner, W., 2016. Mapping rice extent and cropping scheme in the Mekong Delta using Sentinel-1A data. Rem. Sens. Lett. 7 (12), 1209–1218.

Pacheco, A., McNairn, H., Li, Y., Lampropoulos, G., Powers, J., 2016. Using RADARSAT-2 and TerraSAR-X satellite data for the identification of canola crop phenology. In: Remote Sensing for Agriculture, Ecosystems, and Hydrology XVIII. 9998. International Society for Optics and Photonics, pp. 999802.

Periasamy, S., 2018. Significance of dual polarimetric synthetic aperture radar in biomass retrieval: an attempt on Sentinel-1. Remote Sens. Environ. 217, 537–549.

Raney, R.K., Cahill, J.T., Patterson, G.W., Bussey, D.B.J., 2012. The m-chi decomposition of hybrid dual-polarimetric radar data with application to lunar craters. J. Geophys. Res. 117 (E12).

Shirvany, R., Chabert, M., Tourneret, J.-Y., 2012. Estimation of the degree of polarization for hybrid/compact and linear dual-pol SAR intensity images: principles and applications. IEEE Trans. Geosci. Remote Sens. 51 (1), 539–551.

Singha, M., Dong, J., Zhang, G., Xiao, X., 2019. High resolution paddy rice maps in cloud-prone Bangladesh and Northeast India using Sentinel-1 data. Scientific Data 6 (1), 26.

Szigarski, C., Jagdhuber, T., Baur, M., Thiel, C., Parrens, M., Wigneron, J.-P., Piles, M., Entekhabi, D., 2018. Analysis of the radar vegetation index and potential improvements. Remote Sens. 10 (11), 1776.

Touzi, R., Hurley, J., Vachon, P.W., 2015. Optimization of the degree of polarization for enhanced ship detection using polarimetric RADARSAT-2. IEEE Trans. Geosci. Remote Sens. 53 (10), 5403–5424.

Touzi, R., Omari, K., Sleep, B., Jiao, X., 2018. Scattered and received wave polarization optimization for enhanced peatland classification and fire damage assessment using polarimetric PALSAR. IEEE J. Select. Topics Appl. Earth Observ. Rem. Sens. 11 (11), 4452–4477.

Trudel, M., Charbonneau, F., Leconte, R., 2012. Using RADARSAT-2 polarimetric and ENVISAT-ASAR dual-polarization data for estimating soil moisture over agricultural fields. Can. J. Remote. Sens. 38 (4), 514–527.

Ulaby, F., 1975. Radar response to vegetation. IEEE Trans. Antennas Propag. 23 (1), 36–45.

Van Tricht, K., Gobin, A., Gilliams, S., Piccard, I., 2018. Synergistic use of radar Sentinel-1 and optical Sentinel-2 imagery for crop mapping: a case study for Belgium. Remote Sens. 10 (10), 1642.

Veloso, A., Mermoz, S., Bouvet, A., Le Toan, T., Planells, M., Dejoux, J.-F., Ceschia, E., 2017. Understanding the temporal behavior of crops using Sentinel-1 and Sentinel-2-like data for agricultural applications. Remote Sens. Environ. 199, 415–426.

Vreugdenhil, M., Wagner, W., Bauer-Marschallinger, B., Pfeil, I., Teubner, I., Rüdiger, C., Strauss, P., 2018. Sensitivity of Sentinel-1 backscatter to vegetation dynamics: an Austrian case study. Remote Sens. 10 (9), 1396.

Wang, H., Magagi, R., Goita, K., 2016. Polarimetric decomposition for monitoring crop growth status. IEEE Geosci. Remote Sens. Lett. 13 (6), 870–874.

Whelen, T., Siqueira, P., 2018. Time-series classification of Sentinel-1 agricultural data over North Dakota. Rem. Sens. Lett. 9 (5), 411–420.

Wigneron, J.-P., Pardé, M., Waldteufel, P., Chanzy, A., Kerr, Y., Schmidl, S., Skou, N., 2004. Characterizing the dependence of vegetation model parameters on crop structure, incidence angle, and polarization at L-band. IEEE Trans. Geosci. Remote Sens. 42 (2), 416–425.

Wiseman, G., McNairn, H., Homayouni, S., Shang, J., 2014. RADARSAT-2 polarimetric SAR response to crop biomass for agricultural production monitoring. IEEE J. Select. Topics Appl. Earth Observ. Rem. Sens. 7 (11), 4461–4471.

de Wit, A., Duveiller, G., Defourny, P., 2012. Estimating regional winter wheat yield with WOFOST through the assimilation of green area index retrieved from MODIS observations. Agric. For. Meteorol. 164, 39–52.

Wu, L.-K., Moore, R.K., Zoughi, R., 1985. Sources of scattering from vegetation canopies at 10 GHz. IEEE Trans. Geosci. Remote Sens. GE-23 (5), 737–745.